Reviews in Mineralogy & Geochemistry
Vol. 89 pp. 103-145, 2023

Magmatic Evolution I: Initial Differentiation of the Moon

Amy M. Gaffney[*,1], Juliane Gross[*,2,3,4,5], Lars E. Borg[1], Kerri L. Donaldson Hanna[6,7], David S. Draper[8], Nick Dygert[9], Lindy T. Elkins-Tanton[10], Kelsey B. Prissel[11,12], Tabb C. Prissel[4,5], Edgar S. Steenstra[12,13,14], Wim van Westrenen[13]

[1]Nuclear and Chemical Sciences Division, Lawrence Livermore National Laboratory, Livermore, CA 94550, USA
gaffney1@llnl.gov, borg5@llnl.gov

[2]Department of Earth and Planetary Sciences, Rutgers, The State University of New Jersey, Piscataway, NJ 08854, USA
jgross@eps.rutgers.edu

[3]Department of Earth and Planetary Sciences, The American Museum of Natural History, New York, NY 10024, USA
[4]Lunar and Planetary Institute, Universities Space Research Association, Houston, TX 77058, USA
[5]Astromaterials Research and Exploration Science Division, NASA Johnson Space Center, Houston, TX, 77058, USA
tabb.c.prissel@nasa.gov

[6]Atmospheric, Oceanic and Planetary Physics, University of Oxford, Oxford OX1 3PU, UK
[7]Department of Physics, University of Central Florida, Orlando, FL 32816, USA
kerri.donaldsonhanna@ucf.edu

[8]Office of the Chief Scientist, NASA Headquarters, Washington, DC 20546, USA
david.draper@nasa.gov

[9]Department of Earth and Planetary Sciences, University of Tennessee, Knoxville, TN 37996, USA
ndygert1@utk.edu

[10]School of Earth and Space Exploration, Arizona State University, Tempe, AZ, USA
lelkinst@asu.edu

[11]Department of Earth and Planetary Sciences, Washington University in St. Louis, St. Louis, MO 63130, USA
[12]Earth and Planets Laboratory, Carnegie Institution for Science Washington, DC 20015, USA
kelsey.prissel@nasa.gov

[13]Department of Earth Sciences, Vrije Universiteit Amsterdam, Amsterdam, The Netherlands
w.van.westrenen@vu.nl

[14]Institute of Mineralogy, University of Münster, 48149 Münster, Germany
esteenst@uni-muenster.de

**Designates chapter co-leads and corresponding authors*

1529-6466/23/0089-0003$05.00 (print)
1943-2666/23/0089-0003$05.00 (online)
http://dx.doi.org/10.2138/rmg.2023.89.03

1. THE CASE FOR A LUNAR MAGMA OCEAN

In this chapter, we present and discuss in detail current and novel advances in our understanding of the processes that drove primordial differentiation of the Moon. This chapter focuses on four avenues of study: 1) data and observations generated from remote sensing missions, 2) experimental investigations of magma ocean crystallization processes, 3) physiochemical modeling of magma ocean processes, and 4) chronological constraints on lunar differentiation. Investigations completed over the past decade and a half provide results that allow for continued testing of the lunar magma ocean (LMO) hypothesis. Although much of the recent work provides constraints on the processes that may have operated during solidification of a global magma ocean, some investigations also reveal inconsistencies and present challenges to the magma ocean model as it currently stands. These integrated results demonstrate a complex geologic history of our Moon and highlight key areas for future investigation into the initial differentiation of the Moon.

The magma ocean model of primordial lunar differentiation was proposed following the U.S. Apollo 11 mission in 1969 (Smith et al. 1970; Wood et al. 1970) and further developed following the return of ~382 kg of rock and soil samples from the lunar surface by this and the following Apollo missions along with some few grams of rocks and soil returned by the Soviet Luna missions (see Shearer et al. 2006 for detailed reviews). Analyses of these rocks and soil samples, which represent the central and eastern nearside of the Moon, orbital XRF data obtained by Apollo 15 and 16, and interpretation of experimental data from the Apollo Lunar Surface Experiments Package (ALSEP) that was deployed on the lunar surface, identified anorthositic and basaltic rocks as key lithologic constituents. The ferroan anorthositic (FAN) samples contain > 90% plagioclase, with high An# of 94–98 (An# = 100 × molar Ca/[Ca+Na+K]) and interstitial mafic minerals such as olivine and pyroxene with moderate Mg#s, ranging from about 40 to 70 (Mg# = 100 × molar Mg/[Mg + Fe]). The Apollo mare basalts are variably enriched in Ti and strongly depleted in Eu. Relevant experiments demonstrated that plagioclase was not residual in the mare basalt sources, and therefore the Eu depletion indicates that plagioclase had been removed from their source region(s), and that the source region(s) may be complementary to the FANs (e.g., Warren 1985). Analysis of the returned lunar samples also revealed a geochemical component, termed KREEP, that is enriched in incompatible (and heat-producing) elements including potassium (K), the rare earth elements (REE), and phosphorous (P). Based on these compositional observations and the assumption that FAN was globally distributed, the lunar magma ocean (LMO) hypothesis was developed. This model predicts that the Moon was wholly or mostly molten early in its history and during crystallization it differentiated to form, in its simplest structure, a small dense core, a chemically stratified mantle consisting of Mg- and Fe-rich silicate cumulates and Ti-rich ilmenite bearing cumulates, a low-density feldspathic crust, and an incompatible element enriched residuum of crystallization (e.g., Shearer et al. 2006 and references therein).

In the decades since it was first proposed, the LMO model has been further refined. The results of geochemical and chronological analyses of a wide variety of lunar samples, combined with the results of experiments and numerical models designed to elucidate the magma ocean crystallization process, as well as data obtained by remote sensing, have been used to develop a mature model for lunar differentiation through magma ocean crystallization. At the time of writing of the first *New Views of the Moon* volume in the 2000s, the LMO model predicted that Mg-rich olivine and orthopyroxene crystallized first, followed by clinopyroxene, and these mafic minerals sank to form a cumulate mantle (e.g., Solomon and Longhi 1977; Tonks and Melosh 1990; Snyder et al. 1992; Longhi 2003). After ~75–80% of the LMO had solidified, anorthitic plagioclase began to crystallize and floated in the dense Fe-rich melt to form a thick global anorthositic crust enriched in plagiophile elements and characterized by a positive Eu anomaly (chondrite-normalized) and overall low abundances of incompatible trace elements

(e.g., O'Hara and Niu 2015; Gross and Joy 2016). The Eu-depleted residual melt trapped between the mafic cumulates of the lunar mantle and the crustal anorthosites continued to become increasingly enriched in Fe and other elements such as Ti, and crystallized to yield abundant ilmenite after about 95% solidification (Snyder et al. 1992). This Eu-deficient and ilmenite-rich material, together with Fe-rich silicate cumulates, is involved as a source component for subsequent mare basalt magmatism (Snyder et al. 1992; Shearer et al. 2006). After >99% solidification, the residual melt was highly enriched in incompatible elements including Th, K, REE, and P; this residual melt is defined as urKREEP. Traces of this residual melt appear in lunar rocks as the geochemical KREEP component (Warren and Wasson 1979; Snyder et al. 1995; Shearer et al. 2006; Taylor and McLennan 2009). Density-driven mantle overturn and mixing (e.g., Shearer and Papike 1999) was postulated to lead to the onset of secondary magmatism of the highlands high-magnesian suite (Mg-suite, or HMS) and the highlands alkali suite (HAS), both of which can contain a KREEP component (Shearer and Papike 2005; Shearer et al. 2006; Gross et al. 2020).

1.1. Challenges to the lunar magma ocean model and potential alternatives

Over the past 15 years, the magma ocean model has continued to evolve. Although the majority of the recent investigations support and refine the LMO model, others question whether this mechanism alone is responsible for the primordial differentiation of the Moon (Gross and Joy 2016; Pernet-Fisher and Joy 2016; Moore et al. 2017). A major focus area of the past decade has been in characterizing the global compositional variability of the Moon's crust (see Elardo et al. 2023, this volume). Ferroan anorthositic suite rocks (FAS), Mg-suite rocks, and KREEPy material are widespread among the Apollo sites, and are present to some extent at all sample return sites (e.g., Simon and Papike 1985; Gross et al. 2014; Gross and Joy 2016). Investigations of these feldspathic crustal materials revealed compositional variations within the FAS samples that suggest that processes other than flotation during LMO crystallization may also be involved in FAS petrogenesis (e.g., Warren 1990; Jolliff and Haskin 1995; Nyquist et al. 2006; Gross et al. 2014). Furthermore, Sm–Nd chronologic investigations of some FAS samples suggest they are derived from sources that are as depleted in light rare earth elements (LREE) as the most refractory mare basalt sources (Borg et al. 2014). This is improbable within the context of the LMO model even if the Moon originally had a non-chondritic bulk Sm/Nd ratio as suggested by Boyet and Carlson (2007). Orbital remote sensing of areas not sampled by Apollo missions shows that the Moon's highland crust is indeed anorthositic (e.g., Lucey 2004; Prettyman 2006; Greenhagen et al. 2010; Yamamoto et al. 2012; Peplowski et al. 2016), with more recent global datasets showing outcrops of "pure anorthosites" (i.e., regoliths and rocks with <2% Fe-bearing mafic minerals) observed in central peaks and peak rings of craters (Hawke et al. 2003; Ohtake et al. 2009; Yamamoto et al. 2012; Donaldson Hanna et al. 2014), which are consistent with a simple plagioclase flotation crust. However, recent measurements indicate that the Moon's highland crust is compositionally heterogeneous, and that the farside highlands are more magnesian relative to the feldspathic terrane on the nearside (see Elardo et al. 2023, this volume).

The earlier interpretations of Apollo samples were made from a dataset that is geographically restricted to what we now know to be a geochemically atypical region, with enhanced concentrations of KREEP (Jolliff et al. 2000; Korotev 2005), the so called Procellarum KREEP Terrane (PKT) on the lunar nearside. This KREEP geochemical signature, one of the predicted global products of the LMO, is not globally distributed but instead is mostly localized and closely associated with impact ejecta from the nearside Imbrium impact basin (Elphic et al. 2000; Haskin et al. 2000; Lawrence et al. 2003; Gillis et al. 2004). Recently, studies have shown that KREEP-free Mg-suite rocks might exist outside the PKT and thus, that KREEP was not a required component for Mg-suite magmatism (e.g., Korotev et al. 2003; Takeda et al. 2006; Gross et al. 2020). Recent studies have also shown that Apollo highlands crustal samples

all are affected by the contiguous ejecta of the Imbrium basin (Warren 1990; Haskin et al. 2003; Spudis et al. 2011). Thus, the Apollo samples do not represent the full range of the Moon's geological record. Crystallization ages of Apollo FAS samples span 200 m.y. (Borg et al. 2015, and references therein), whereas some thermal models of LMO formation predict that the LMO may have solidified in as few as tens of millions of years (e.g., Elkins-Tanton et al. 2011). Similarly puzzling are other radiometric ages of FAS samples that overlap with those of the Mg-suite rocks (Borg et al. 2015, and references therein), even though the LMO model predicts that Mg-suite rocks formed after the anorthositic crust was stabilized. Detailed investigations of Apollo samples, new meteorite samples (see Joy et al. 2023, this volume), and novel volatile element measurements (see McCubbin et al. 2023, this volume), have brought to light a diversity of anorthositic clast lithologies and rock types such as Mg-anorthosites (MAN) that seem to have no obvious origin in the simple LMO model (e.g., Korotev et al. 2003; Takeda et al. 2006; Treiman et al. 2010; Gross et al. 2014), although Charlier et al. (2018) offer some explanations. For more details see Elardo et al. (2023, this volume).

Recent detailed investigations of the major, minor and trace element abundances of anorthosite clasts within lunar meteorites and FAN clasts in Apollo 15 and 16 samples have revealed additional complex geochemical characteristics of anorthosite and showed that it cannot be explained by crystallization from a single magma ocean composition or a single magma source (Gross et al. 2014; Russell et al. 2014; Pernet-Fisher et al. 2019; Tartèse et al. 2019). All these new observations have led to the re-examination of the LMO hypothesis (e.g., Longhi 2003; Borg et al. 2011; Gross et al. 2014; O'Hara and Niu 2015; Gross and Joy 2016; Pernet-Fisher and Joy 2016; Yamamoto et al. 2016; Pernet-Fisher et al. 2019) and development of alternative models for formation of the anorthositic crust and other products attributed to differentiation of the LMO. Some of these hypotheses still necessitate a lunar magma ocean to account for the formation of an olivine and pyroxene rich mantle prior to the onset of plagioclase-rich crust formation, but others propose more complex non-magma ocean models for early lunar differentiation. Some of these alternative models include:

- Heterogeneous accretion and/or magma ocean: in this model, vigorous convection within a magma ocean could have caused asymmetrical aggregation of refractory parental melts or plagioclase flotation mushes, thereby causing crustal thickness and compositional variations between the farside (more magnesian, early precipitates) and nearside (more ferroan, later precipitates) crustal regions (Arai et al. 2008; Yamamoto et al. 2016).
- Serial magmatism: a model in which pods of basaltic magma repeatedly intruded into a preexisting crust, and discrete 'rockberg' plagioclase crystal-mushes buoyantly rose towards the surface as diapirs driven upward by thermal convection, thereby producing compositionally variable anorthosites, including pure anorthosites (e.g., Walker 1983; Longhi 2003, 2006; Korotev et al. 2010; Gross et al. 2014).
- Impact bombardment: these models include large regional melting events (i.e., magma seas) during impact events resulting in the localized occurrence of ferroan anorthosites and KREEP in the PKT (Haskin et al. 1981, 1998; Gross et al. 2014).
- Heat-pipe cooling: in this model, the plagioclase-rich crust is produced and refined through a widespread episode of heat-pipe magmatism (persistent global volcanism) rather than solely produced by density-driven plagioclase flotation (Moore et al. 2017), accounting for the nearly pure plagioclase melts and textures observed in Apollo samples, while at the same time resulting in the variations in Mg contents, and the diversity of materials contained in lunar meteorites (Takeda et al. 2006; for a more detailed summary of alternative crustal formation models see Gross and Joy 2016).

2. GLOBAL DISTRIBUTION OF POTENTIAL PRIMORDIAL DIFFERENTIATION PRODUCTS

Remote sensing observations from across the electromagnetic spectrum provide a global view of the lunar crust and allow for detailed investigations into the vertical and horizontal heterogeneities at the local scale within the crust. These remote investigations expand the application of laboratory studies by placing them in a global context. In addition, both the global- and local-scale remote observations place important compositional and geophysical constraints on the formation of the lunar crust and how it has evolved into what is observed today with modern spacecraft; see Gaddis et al. (2023, this volume) for a comprehensive overview.

2.1. Large scale lunar crustal surface heterogeneity and distinct terranes

Global-scale observations of the lunar surface by Lunar Prospector (LP) and Clementine revealed a hemispheric petrologic and geochemical dichotomy between the lunar nearside and farside, which could have resulted from the primordial crystallization of a global lunar magma ocean, from secondary processes such as mantle overturn, serial magmatism or large impacts, or a combination of primordial and secondary processes. Large-scale geochemical and petrologic provinces identified using geochemical variations apparent from Clementine and LP data include the Procellarum KREEP Terrane (PKT), the South Pole-Aitken Terrane (SPAT), and the Feldspathic Highlands Terrane (FHT) (Jolliff et al. 2000).

The PKT is located on the lunar nearside in the greater Procellarum-Imbrium region, is defined by a contiguous region with > 3.5 ppm Th, and includes low albedo mare and high albedo nonmare units (Jolliff et al. 2000). Remote sensing measurements showed that the PKT has high abundances of the incompatible elements Th, K, and U (Prettyman et al. 2006; Yamashita et al. 2010). The enrichment in these heat-producing elements is hypothesized to indicate the presence at depth of a residual component from the crystallization of the LMO, urKREEP, which was incorporated into lavas now exposed at the surface. The SPAT is located on the farside, and includes the South Pole-Aitken basin, which is the largest (2100–2500 km in diameter) and oldest (pre-Nectarian) impact basin on the Moon (Stuart-Alexander 1978; Spudis et al. 1994). Morrison (1998), Potter et al. (2012), and Vaughan and Head (2013) suggested that the impact creating the basin would have excavated through the crust exposing the lunar mantle, melting significant volumes of material, and creating a large region of impact melt. This is consistent with the observation that, compared to the FHT, SPAT has elevated abundances of Fe, Mg, Ti, Th, K, and U, but has low abundances of the incompatible elements compared to those measured in the PKT (Prettyman et al. 2006; Yamashita et al. 2010). The higher abundances of Mg and Fe in SPAT, as well as global mineralogy derived from Clementine, suggest that SPAT is more mafic than the FHT (e.g., Crites and Lucey 2015).

The FHT is commonly interpreted to be an ancient stable crust that formed as plagioclase crystallized and floated during the late stages of the LMO (Smith et al. 1970; Wood et al. 1970). Global elemental and mineralogical maps derived from LP, Clementine, the Moon Mineralogy Mapper (M^3), and SELENE Multiband Imager (MI) and Spectral Profiler (SP) support this hypothesis because the FHT has been shown to be plagioclase-rich (> 80% plagioclase) and poor in mafic materials (Prettyman et al. 2006; Crites and Lucey 2015; Peplowski et al. 2016). The mafic minerals that are observed in the farside FHT are more magnesian than the mafic minerals observed in returned samples from the lunar nearside (Ohtake et al. 2012; Crites and Lucey 2015) and seem to be more similar to mafic minerals observed in anorthositic clasts in feldspathic meteorites (e.g., Gross et al. 2014; Gross and Joy 2016; Pernet-Fisher et al. 2019). However, it should be noted that the global remote sensing datasets represent the integrated material at the lunar surface, which is megaregolith. Although small pieces of magnesian anorthosite exist in the Apollo and meteorite collections, the magnesian components are not clearly associated with the anorthositic lithologies in lunar meteorites (see Joy et al. 2023, this volume).

2.2. Small scale lunar crustal surface observations

Although the global-scale remote sensing observations provide insight into the large-scale heterogeneities observed across the lunar surface, investigations at the crater-scale are also needed to better identify products of the crystallization of the LMO as well as constrain the horizontal variability and vertical stratigraphy of the crust. Such fresh and nearly regolith-free locations have been found in crater central peaks, walls, ejecta, and impact basin rings. Investigations of these sites using M^3, SP, and MI, as well as high spatial and high spectral resolution visible to near infrared (VNIR) spectrometers on board the Chandrayaan-1 and SELENE spacecraft, have identified evidence for spectrally pure anorthosite (PAN) regions containing > 98% high-purity plagioclase (Ohtake et al. 2009; Yamamoto et al. 2012; Cheek et al. 2013; Donaldson Hanna et al. 2014). Although thermal infrared spectroscopy revealed that the compositions of these PAN outcrops are consistent with plagioclase found in returned samples of FANs ($An_{94–98}$; Warren 1985; Greenhagen et al. 2010; Donaldson Hanna et al. 2014), PAN rocks contain a much higher plagioclase abundance than previously estimated based on the analyses of most pristine Apollo samples, observations from Clementine, and crustal thickness models (e.g., Warren 1990; Wieczorek and Zuber 2001).

PAN outcrops have been identified across all terrane types, including FHT, PKT, and the outer annulus of SPAT and are commonly associated with large impact basins. The combination of the expected excavation depths of the impact basins and craters that would have sampled deep into the lunar crust and the GRAIL crustal thickness models suggest the existence of a thick (~50 km) and widespread PAN layer spanning the entire crustal column (Ohtake et al. 2009; Yamamoto et al. 2012; Donaldson Hanna et al. 2014; Baker and Head 2015). For a more in-depth discussion of PAN formation and occurrence, the reader is referred to Elardo et al. (2023, this volume).

2.3. Remote observations of lateral structure and composition of the exposed lunar surfaces

In an effort to better constrain the lateral crustal heterogeneity and the vertical stratigraphy within the crustal column, surveys of small (< 1 km) and complex craters have been completed (e.g., Cahill et al. 2009; Lucey et al. 2014; Lemelin et al. 2015). A detailed survey of immature craters with diameters less than 1 km characterized the composition and structure of the megaregolith and found that: (1) lithologies exposed in craters within the FHT can be classified as noritic anorthosites (80 ± 5% plagioclase; 20 ± 5% pyroxene, almost all of which is low-Ca pyroxene; and 0 ± 1% olivine) and (2) lithologies exposed in craters within SPA can be classified as norites (56 ± 17% plagioclase; 42 ± 14% pyroxene, 88 to 95 % of which is low-Ca pyroxene and the rest high-Ca pyroxene; and 2 ± 3% olivine; Lucey et al. 2014). To characterize the composition and structure at greater depths within the crust, the central peaks of complex craters have been probed. These studies demonstrated that the vast majority of the central peaks exhibit a substantial compositional diversity, although the scale at which these heterogeneities could be resolved is variable, with spatial scales ranging from 60 m up to 280 m (Cahill et al. 2009; Lemelin et al. 2015; Martinot et al. 2018). Within the FHT, central peaks were identified as anorthosites, noritic/gabbroic anorthosites and anorthositic norites/gabbros; in the PKT, central peaks were identified as noritic/gabbroic anorthosites, anorthositic norites/gabbros, norites/gabbros, and troctolitic anorthosites; and in the SPA, central peaks were identified as anorthositic norites/gabbros and norites/gabbros (Lemelin et al. 2015; Martinot et al. 2020). The mineralogy and rock types identified in central peaks are not systematically correlated with local crustal thickness, central peak depth of origin, or depth of origin relative to the crust–mantle boundary (e.g., Cahill et al. 2009; Lemelin et al. 2015). These results suggest that lateral and vertical mineralogical heterogeneity exists within the lunar crust, at a scale greater than the spatial resolution of the observations.

Vertically heterogeneous distribution of mafic minerals is predicted by physical models evaluating rafting of mafic minerals by buoyant plagioclase in the convecting magma ocean, and the crystallization of trapped liquids within the flotation crust as it formed (Suckale et al. 2012a; Piskorz and Stevenson 2014; Dygert et al. 2017). The most ancient flotation crust would have had the highest proportion of mafic minerals due to rafting during plagioclase flotation and solidification of trapped interstitial melt; younger sections are predicted to have a purity consistent with the remote sensing constraints on the composition of PAN, due to reworking by serial magmatism or exclusion of interstitial melt by compaction (Piskorz and Stevenson 2014; Dygert et al. 2017). Either a well-stratified crust with anorthositic and mafic layers formed and was then re-worked through impact or magmatic processes, or a heterogeneous crust with an anorthosite-rich upper layer formed during the crystallization of the magma ocean. Dygert et al. (2017) proposed redistribution of PAN after magma ocean crystallisation in a process akin to serial magmatism (e.g., Walker 1983; Jolliff et al. 2000; Longhi 2003; Gross et al. 2014), where deeper, purer portions of the flotation crust intruded into overlying impure crust in a multitude of diapirs.

Detailed VNIR spectroscopy investigations have identified mafic mineral assemblages that may be associated with primordial differentiation products that represent potential lower crustal or upper mantle materials. Outcrops spectrally dominated by low-Ca pyroxene have been identified in the northern Imbrium noritic (NIN) anomaly, the highlands around Mare Frigoris, Bullialdus crater, and SPA basin (e.g., Nakamura et al. 2009; Klima et al. 2011; Kramer et al. 2013; Moriarty et al. 2013). The modified Gaussian model of orthopyroxene spectra suggests that those deposits north of Mare Frigoris have moderate Mg contents (Mg# 50–75), similar to those found in association with highly calcic plagioclase in typical FAN rocks (Klima et al. 2011). The orthopyroxenes identified south of Mare Frigoris, around the rim of Mare Imbrium, and in Bullialdus crater, are more Mg-rich (Mg# >75) (Klima et al. 2011). These orthopyroxene identifications may represent exposures of Mg-suite intrusions (Klima et al. 2011). These exposures are co-located with elevated Th abundances, consistent with the KREEP signature observed in returned samples of Mg-suite rocks (Klima et al. 2011). Within SPA basin, most low-Ca pyroxene exposures are associated with norite and have Mg#s that range from 50–75 (Nakamura et al. 2009; Klima et al. 2011; Moriarty et al. 2013). Analyses of outcrops on the central peaks of craters in SPA identified both Mg- and Fe-rich orthopyroxene across the basin. Their spatial distribution implies the presence of an extensive orthopyroxene-rich layer beneath SPA that formed either from the differentiation of an impact melt sheet (Hurwitz and Kring 2014; Vaughan and Head 2014) or from significant fractional crystallization of the LMO prior to the onset of plagioclase flotation (Nakamura et al. 2009; Moriarty et al. 2013). In addition to low-Ca pyroxene, high-Ca pyroxene has been identified throughout the highlands in bright-rayed craters between 8 and 24 km in diameter (Ogawa et al. 2011) and in the central peaks of craters (Lemelin et al. 2015; Martinot et al. 2018, 2020), suggesting that these materials originated either from mixing with a deep gabbroic layer formed during original LMO crystallization, or via the excavation of a gabbroic pluton formed during secondary magmatism.

Olivine-bearing outcrops have been identified in concentric rings around basins (SPA, Imbrium, Crisium, Humorum, Nectaris, Serenitatis, Humboldtianum, Australe and Moscoviense), as well as near Roche and Tsiolkovsky craters (Yamamoto et al. 2010; Kramer et al. 2013; Corley et al. 2018). Thermal infrared observations and radiative transfer modelling have constrained the abundance of olivine in these outcrops to range from 12 to 87% and 3 to 35%, respectively (Arnold et al. 2016; Corley et al. 2018). These results suggest that some of the olivine-bearing outcrops are troctolitic in composition, which could indicate formation as LMO crystallization products in the mantle or lower crust, a differentiated impact-melt sheet, or olivine-bearing plutons in the lower crust (e.g., Arnold et al. 2016; Corley et al. 2018).

These recently obtained remote sensing datasets have revealed the complex makeup of the Moon's crust and will help to test the LMO paradigm and models of crust formation. The results highlighted here point to several avenues of future remote sensing investigations and demonstrate that coordinated observations across a wide spectral range and returned (as well as future returned) lunar sample collections are needed at the local scale (e.g., spatial resolutions on the order of meters) to (1) better constrain the source regions of olivine-bearing materials and (2) better understand how and if these geochemical provinces are directly related to the crystallization of the LMO or result from secondary processes including mantle overturn, large impacts and/or magmatism.

3. EXPERIMENTAL CONSTRAINTS ON MAGMA OCEAN SOLIDIFICATION

Experimental investigations of the conditions of magma ocean crystallization completed over the past decade have produced extensive, internally consistent datasets that cover the likely range of bulk LMO compositions, fO_2, and crystallization histories (i.e., equilibrium vs. fractional crystallization). These studies increase our understanding of LMO solidification processes, post-LMO magmatism, and provide new constraints for future efforts to model LMO solidification and subsequent lunar evolution. These experiments build upon numerical models, such as those of Longhi (1991), Snyder et al. (1992), Elkins-Tanton et al. (2011), and Davenport (2013), which were developed to simulate the crystallization sequence of a cooling magma ocean and the resulting lithologic units, and provide data from which to build the next generation of numerical models (discussed in the following section). Below, we outline the rationales for the choice of starting compositions, the conditions and types of crystallization, the key phase equilibria from each set of experiments, and how the experimental results compare both to each other and to the predictions of numerical models.

3.1. Lunar magma ocean bulk composition

Some of the studies discussed in this section aimed to experimentally test the "two-stage process" numerical model of Snyder et al. (1992), in which crystals and liquid remain in contact, and thus in equilibrium, during solidification (perhaps owing to sufficiently vigorous convection or inefficient crystal settling that would suspend early-formed crystals), followed by fractional crystallization of the residual magma ocean in which crystals are removed from the system as they form (e.g., Elardo et al. 2011; Lin et al. 2017a,b, 2019). Others have incorporated aspects suggested by "one-stage process" numerical models (e.g., Elkins-Tanton et al. 2011), in which fractional crystallization operated throughout the solidification process (Charlier et al. 2018; Rapp and Draper 2018). It remains an open question whether the Moon was wholly molten prior to differentiation or whether some unmelted, primordial lunar mantle remains in the deep interior, although most recent assessments of the temperatures associated with Moon formation (Canup et al. 2023, this volume) and subsequent core formation (see following section) are more consistent with whole-Moon melting. In any case, all experiments designed to constrain the evolution of the LMO must begin by assuming a composition for the bulk silicate Moon.

Several bulk LMO compositions have been utilized in crystallization experiments. These starting compositions were chosen to represent the bulk silicate Moon, that is, the composition of the bulk Moon immediately after the formation of the lunar core. The composition of the Moon has been difficult to establish for almost 50 years now and has varied greatly in estimates (see Taylor et al. 2006, for an in-depth discussion). Starting compositions for experimental investigations (Table 1) include: Taylor Whole Moon (TWM; Taylor 1982) with ~6 wt. % Al_2O_3 and Mg# = 84; a depleted Lunar Primitive Upper Mantle (LPUM; Longhi 2003, 2006; Shearer et al. 2006) with ~4 wt. % Al_2O_3 and Mg# = 90; a composition derived via inversion of lunar seismic data (Khan et al. 2007) with 4.5 wt. % Al_2O_3 and Mg# = 86; and a bulk composition with 3.9 wt. % Al_2O_3 and Mg# = 83 (O'Neill 1991). TWM includes

~50% enrichment of refractory elements, such as Al and Th, relative to Earth (Taylor et al. 2006), whereas LPUM represents no refractory element enrichment. Note that in the modeling of Snyder et al. (1992), a composition modified from that of Buck and Toksöz (1980) with 5 wt. % Al_2O_3 and Mg# 82 was used, which is consistent with the emerging consensus on the compositional similarity between the Moon and Earth (e.g., Qin et al. 2010; Zhang et al. 2012; Young et al. 2016; Mougel et al. 2018).

Table 1. Estimated bulk compositions of the Moon.

	TWM	**LPUM**	**R76**	**M78**	**BT80**	**WD84**	**R87**	**R87**	**O91**	**S92**	**K07**
SiO_2	44.40	46.10	46.00	42.41	48.37	44.20	43.24	44.21	44.60	48.40	45.50
TiO_2	0.31	0.17	0.20	0.38	0.40	–	0.30	0.42	0.17	0.40	0.53
Al_2O_3	6.10	3.90	3.90	7.43	5.00	3.76	3.72	5.18	3.90	5.00	4.50
Cr_2O_3	0.61	0.50	0.40	0.29	0.30	0.37	0.32	0.36	0.47	0.30	–
FeO^T	10.90	7.60	8.20	12.70	12.90	12.70	12.24	13.54	12.40	12.00	10.50
MnO	0.15	0.13	–	0.15	–	0.16	0.16	0.18	0.17	–	–
MgO	32.70	38.30	38.10	28.49	29.02	35.50	36.85	31.85	35.10	29.90	35.70
CaO	4.60	3.20	3.10	6.01	3.83	3.15	3.03	4.18	3.30	3.80	3.20
Na_2O	0.09	0.05	0.10	0.10	0.15	–	0.06	0.08	0.05	0.13	–
K_2O	0.01	0.00	–	0.01	–	–	–	–	–	0.04	–
Total	99.87	99.95	100.00	97.96	99.97	99.84	99.92	100.00	100.16	99.97	99.93
Mg#	84	90	89	80	80	83	84	81	83	82	86

Notes: TWM: Taylor Whole Moon; LPUM: Lunar Primitive Upper Mantle; R76: Ringwood (1976); M78: Morgan et al. (1978); BT80: Buck and Toksöz (1980); WD84: Wänke and Dreibus (1984); R87: Ringwood et al. (1987); O91: O'Neill (1991); S92: Snyder et al. (1992); K07: Khan et al. (2007).

3.2. Conditions and modes of crystallization

Lunar magma ocean crystallization has been conceptually modeled as one of two differentiation sequences, and experimental studies have been conducted to mimic both the one-stage and the two-stage process. Combined with use of the starting and bulk materials described above, these experiments were run at fO_2 ranging from approximately IW to IW + 1.5 and span the likely range of physical processes thought to have formed the Moon from an initial magma ocean.

For both equilibrium and fractional types of experiments, the starting material is held at a temperature and pressure of interest, allowing solid phases to crystallize and equilibrate with the melt. The experimental run products are used to determine the stability of phases over relevant pressure-temperature conditions. The solid phase assemblage from each experiment is taken to represent the likely lithological products capable of accumulating, whereas melt compositions from each experiment are taken to represent a liquid line of descent. In an equilibrium crystallization sequence, a single starting composition is used for experiments at different temperature and pressure conditions and the experiments simulate crystals and liquid that remain in contact until some critical extent of crystallization. In contrast, a fractional crystallization sequence mimics a situation where crystals settle shortly after they form, removing those components from the system. Fractional crystallization experiments follow a pressure–temperature crystallization path similar to the schematic illustration in Figure 1, and the starting composition for each fractional crystallization step is defined by the melt

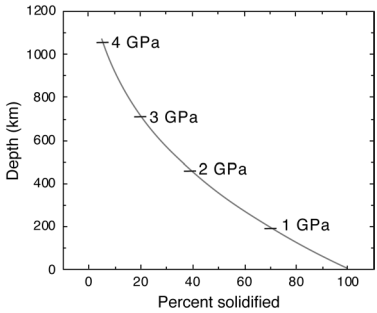

Figure 1. Calculated depth vs. percent of Moon solidified during fractional crystallization. Curve labeled with approximate pressures at various depths.

composition of the preceding (higher-temperature) experiment. For both equilibrium and fractional experimental crystallization sequences, the phases and compositions of accumulated crystals correspond to the growing cumulate pile, and the subsequent solidification depends on the compositions of residual liquids.

LMO solidification is modeled primarily as a "bottom up" process, by which the lunar interior is filled up with the crystals accumulated during LMO crystallization. However, it is likely that LMO cooling would have been promoted by exposure to space at the lunar surface and impeded by the presence of a conductive lid or plagioclase flotation crust (e.g., Elkins-Tanton et al. 2011). In most models of LMO solidification, anorthitic plagioclase feldspar eventually joins the crystallizing assemblage. Plagioclase is buoyant relative to coexisting liquid (Walker and Hays 1977), leading to formation of a plagioclase-rich flotation crust. Some studies (Snyder et al. 1992; Elkins-Tanton et al. 2011; Nekvasil et al. 2015) used numerical models to estimate that the onset of plagioclase saturation in a crystallizing LMO occurred near 78 to 80 vol.% solidification, denoted 'PCS' hereafter (PCS = Per Cent Solid), though readers should note that some experimental studies report liquid and solid fractions in wt.% (e.g., Charlier et al. 2018; Rapp and Draper 2018). Further, numerical models predict that later-formed cumulate lithologies would be more Fe-rich and hence denser than those formed earlier, leading to gravitational instability that could cause overturn during or immediately after the final stages of LMO crystallization (e.g., Hess and Parmentier 1995; Maurice et al. 2017; Boukaré et al. 2018; Li et al. 2019; Maurice et al. 2020). The experiments reviewed here simulate LMO solidification before the onset of any subsequent overturn, and thus, can provide fundamental inputs to flotation and overturn models.

3.3. Simulating two-stage crystallization

Elardo et al. (2011) and Lin et al. (2017a,b, 2019) performed two-stage equilibrium crystallization experiments using different starting compositions and slightly different experimental approaches. Elardo et al. (2011) simulated a nominally dry magma ocean having an adiabatic thermal profile using experiments conducted over a range of covarying temperatures and pressures. In contrast, Lin et al. (2017a,b) conducted experiments in sets at a given temperature, and at a range of pressures, to mimic crystallization in an isothermal magma ocean in which interior pressures vary as a function of depth. Further, Lin et al. (2017a, 2019) reported experimental results of a hydrous magma ocean, whereas Lin et al. (2017b) reported integrated, weighted average compositions of nominally dry residual LMO liquids and cumulate mineral assemblages that drew data from the pressure range covered at each experimental temperature. In the Elardo et al. (2011) experiments, the pressure was held constant over a range of temperatures. Although Elardo et al. (2011) reported results for both TWM (refractory enriched) and LPUM LMO bulk compositions up to >70% PCS, and modeled processes at more advanced degrees of crystallinity, Lin et al. (2017a,b, 2019) reported results of two-stage experiments that covered more complete LMO solidification using the geophysically

constrained bulk composition proposed by Khan et al. (2007). In those experiments, the transition from equilibrium to fractional crystallization was imposed at 50% PCS.

In the Elardo et al. (2011) experiments, the TWM produced a high-pressure cumulate assemblage that contains trace Cr-spinel in addition to Al-bearing low-Ca pyroxene and olivine. Garnet also crystallized at 4 GPa (~9%), but according to the physical model that was simulated, the authors conclude it would not occur in the lunar mantle. In contrast, LPUM produced a high-pressure dunitic cumulate assemblage with low-Ca pyroxene but without an aluminous phase. The differences in bulk composition are magnified in the residual melt; the residual LMO from the TWM composition is more plagioclase- and ilmenite-normative than is that from LPUM. These experimental results indicate that both compositions could produce Mg-rich early cumulate piles that extend from the core–mantle boundary to ~355 km depth, if 50% equilibrium crystallization and whole Moon melting are assumed. Elardo et al. (2011) argued that these early LMO cumulates could provide the source regions for a component of the magmas parental to the Mg-suite cumulates that have high-Mg# and are Ni- and Co-poor. Mixing of these cumulates with urKREEP and crustal plagioclase is required to produce the Al and incompatible element characteristics of the Mg-suite magmas. The olivine in early LMO cumulates produced by either bulk Moon composition is far too rich in Cr to match the source regions of the Mg-suite.

In the Lin et al. (2017b) experiments using the Khan bulk composition, olivine + orthopyroxene crystallized during the first 70% of solidification (including the transition to fractional crystallization at 50 PCS; Figs. 2, 3). Plagioclase joined the assemblage at about 68 PCS, and olivine stopped crystallizing after about 82 PCS. Late-stage liquids were Fe-rich and ilmenite-saturated. Lin et al. (2017b) argued that their results indicate that a dry LMO would generate a feldspathic crust ~67 km thick, which is greater than the crustal thickness range of 34-43 km estimated from GRAIL mission data (Wieczorek et al. 2013). Lin et al. (2017a, 2019) showed that an initial LMO containing water would crystallize plagioclase later in the sequence, and produce overall less plagioclase, resulting in an estimated crustal thickness in agreement with GRAIL observations. In the water-bearing experiments, olivine ± orthopyroxene crystallized until 68 PCS, and plagioclase did not crystallize until ~71 to 73 PCS. From ~89 to 95 PCS, silica, spinel, and high-Ca pyroxene crystallized with plagioclase and ilmenite. Lin et al. (2019) quantified the H_2O contents of the experimental charges of Lin et al. (2017a) via SIMS measurements and determined their hydrous experiments contained up to ~0.6 wt. % H_2O, approximately a factor of three lower than initially estimated. Lin et al. (2019) used their hydrous results to calculate initial LMO water contents of 90, 325, 410, 220, and 240 ppm H_2O if the LMO had initial depths of 400, 700, 1000, 1200, or 1350 km, respectively.

3.3.1. Key comparisons among the two-stage experimental studies. Lunar researchers using the experimental results summarized here should bear in mind several important distinctions between these studies. First, the Elardo et al. (2011) piston–cylinder experiments were run in unsealed graphite capsules within talc–Pyrex cell assemblies, and the talc sleeves in such experiments commonly dehydrate, which can allow water to migrate, possibly into the sample capsules. However, the experiments were not analyzed for water content. The experiments of Lin et al. (2017a,b) were conducted in talc cells with sealed Pt capsules, but Pt is very permeable to H so this concern also applies to those studies. However, Lin et al. (2019) reported that ~66% of water added to these types of experiments is lost during the run, and the measured water content of their previous experimental charge was approximately a factor of three lower than initially estimated. Second, the LMO bulk composition used by Lin et al. (2017a,b, 2019) lacks Cr, P, and alkalis (Table 1), which limits the evaluation of these results in the context of natural data; e.g., the plagioclase is pure anorthite, the stability of Cr-spinel and its aluminum content cannot be fully addressed, and a P-free composition hampers the ability to assess the role of late-forming phosphates in the high-PCS residual LMO liquids, which are expected to represent KREEP. The studies by Lin et al. (2017a, b) produce a silica phase

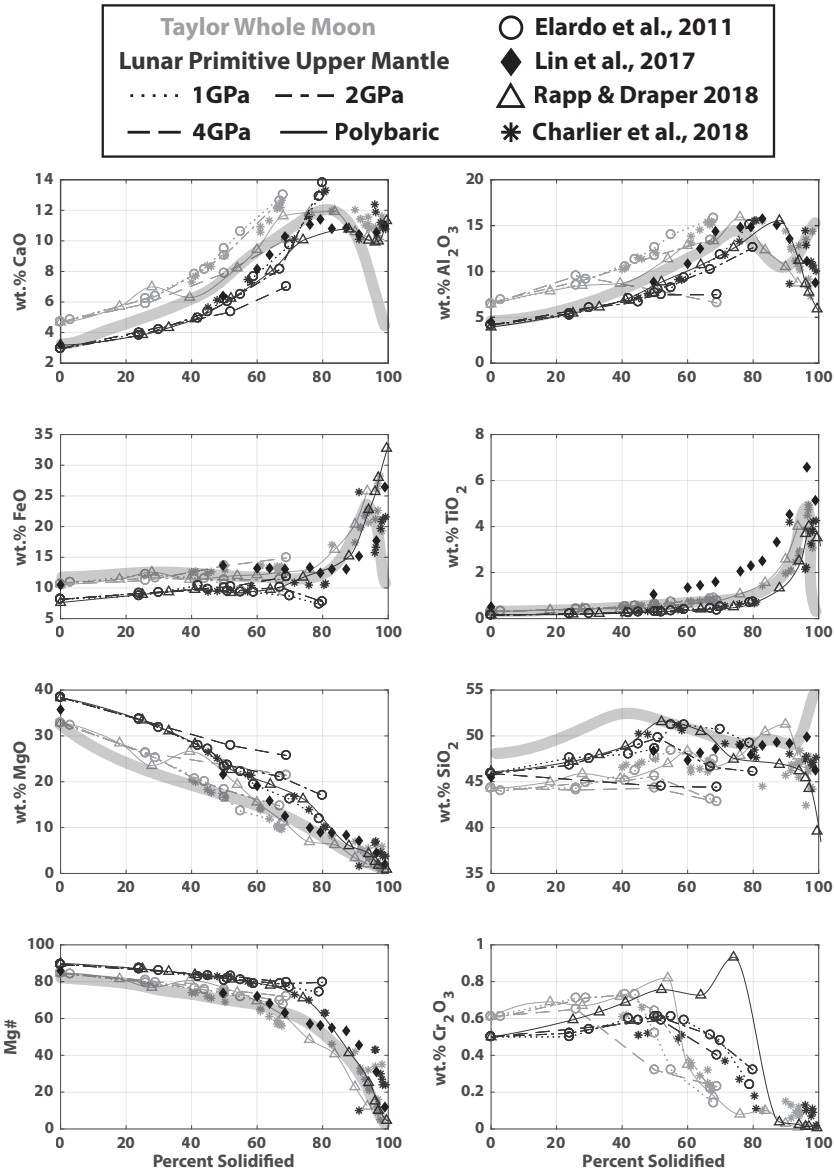

Figure 2. Chemical evolution of residual LMO liquids during experimental crystallization with percent solidified compared to numerically determined LMO liquid line of descent at 0.6 GPa from Snyder et al. (1992; smooth **grey curves**, hereafter Snyder model). Results for TWM in **filled circles and curves** (Elardo et al. 2011; Rapp and Draper 2018), LPUM in **filled squares and curves** (Elardo et al. 2011; Rapp and Draper 2018), and those of Lin et al. (2017) in **black diamond symbols**. Equilibrium crystallization for ~80 PCS followed by fractional crystallization is used by the Snyder model. Both TWM and LPUM experiments were temperature sequences at 1 GPa, 2 GPa, and 3 GPa, whereas Lin et al. (2017) used a polybaric approach; both groups mimicked "bottom up" crystallization of the LMO. Rapp and Draper (2018) simulated fractional crystallization from the onset and assumed whole-Moon melting, whereas Lin et al. (2017) assumed a LMO ~700 km deep. See text for additional discussion.

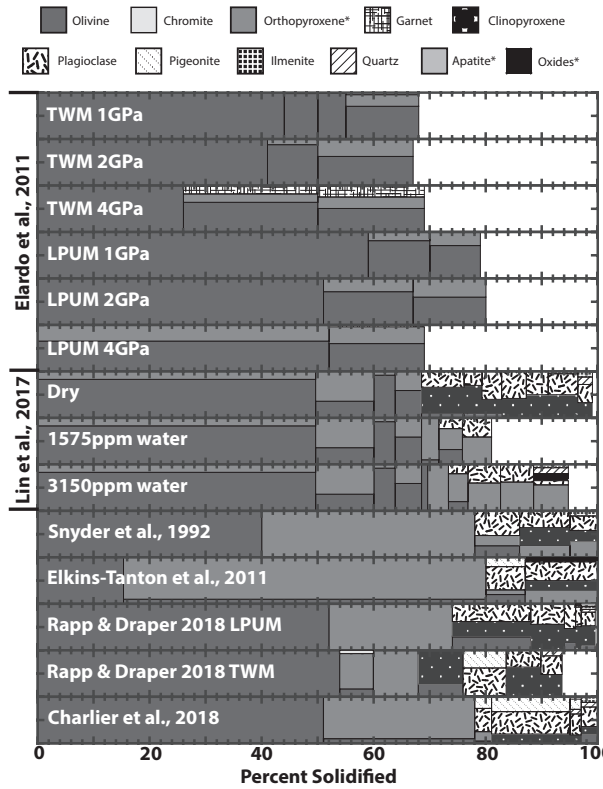

Figure 3. Comparison of experimentally-determined LMO crystallization sequences and cumulate products to the numerical model of Snyder et al. (1992) (0.6 GPa). Results for TWM and LPUM are from Elardo et al. (2011) and Rapp and Draper (2018). Lin et al. (2017a,b, 2019) results use the Khan et al. (2007) bulk composition. Charlier et al. (2018) results use the LPUM bulk composition. Orthopyroxene* is shown in both Snyder et al. (1992) and Lin et al. (2017a,b, 2019) and is reported as a single-phase pyroxene. The composition of spinel (oxide*) is not reported in Lin et al. (2017). Apatite* is reported in Rapp and Draper (2018).

at the final stages of crystallization. This is an interesting result, as silica-rich phases are not abundant in crustal rocks and silica-rich lithologies are uncommon rather than a widespread component of the lunar crust. However, these experimental products could represent very end stage liquids that would be trapped beneath the crust and therefore present the compelling possibility that they may be a precursor for lunar granites (Lin et al. 2017a,b, 2019).

3.4. Simulating one-stage (fully fractional) crystallization

Simulations in which the LMO solidified solely by fractional crystallization have focused on the TWM, LPUM, and O'Neill (1991) bulk compositions (Charlier et al. 2018; Rapp and Draper 2018). These studies pursued the possibility that separation of crystals from the LMO was sufficiently efficient that crystals would not remain in contact with residual liquids. To mimic the fractional crystallization process, the composition of the glass from each step was used as the starting composition for the next set of experiments, thereby simulating a specific percentage of fractionation of crystals from the melt (Villiger et al. 2007). The Rapp and Draper (2018) experiments were run to 0.5 GPa in a piston–cylinder apparatus, and the final ~25% of LMO solidification was simulated at 1-atmospheric pressure using a Deltech CO–CO_2 gas-mixing furnace with oxygen fugacity held at the iron–wüstite buffer. At each high-pressure stage,

the total volume crystallized was used to calculate the pressure appropriate for the next set of experiments (Fig. 1). Charlier et al. (2018) ran sets of isobaric experiments at various temperatures and used the glass composition from one experiment as the starting composition for the next set of experiments run at a lower pressure. In this study, the starting liquid compositions were determined by forward modeling of the TWM, LPUM and O'Neill (1991) bulk compositions to determine the PCS, bulk composition, and pressure at the point of low-Ca pyroxene saturation.

In the Rapp and Draper (2018) experiments, both the TWM and LPUM compositions produced only olivine ($Fo_{90–95}$) during the first 50% of fractional crystallization. In the LPUM composition, only low-Ca (ortho)pyroxene crystallized in the next 25% crystallization, whereas in TWM olivine was joined by orthopyroxene and Cr-spinel. At about 70 PCS, the TWM crystallizing assemblage was olivine + high-Ca (clino)pyroxene, and pigeonite replaced olivine (Figs. 2, 3). Plagioclase ($An_{89–94}$) joined the assemblage at about 75 PCS in both bulk compositions. At 90 PCS, the furthest extent yet accomplished on TWM, the assemblage was plagioclase + clinopyroxene + silica. In LPUM, plagioclase co-crystallized with olivine, orthopyroxene, and clinopyroxene from 75 to ~88 PCS, at which point pigeonite or pigeonite + olivine coexisted with plagioclase. At the highest simulated PCS of ~98 on LPUM, the assemblage was olivine, pigeonite, clinopyroxene, plagioclase, ilmenite, quartz, ulvöspinel, and merrillite.

The Charlier et al. (2018) experiments on the LPUM bulk composition showed olivine + orthopyroxene crystallization to about 78 PCS, at which point pigeonite and plagioclase joined the assemblage (Figs. 2, 3). At 81 PCS, the crystallizing assemblage was pigeonite, augite and plagioclase. In the final 5% of solidification, the crystallizing assemblages were pigeonite + augite + plagioclase + a silica phase, followed by olivine + augite + plagioclase + a silica phase + ilmenite (Figs. 2, 3).

3.5. Comparison of experimental results with numerical model results

Experimental results are compared with each other and with the models of Snyder et al. (1992) and Elkins-Tanton et al. (2011) in Figures 2 and 3. Both of these numerical models are based on a cumulate sequence calculated using the MAGFOX magma ocean crystallization code developed by Longhi (1991). Figures 2 and 3 depict the evolution of LMO liquids and LMO cumulate piles, respectively. A robust conclusion is that the experiments strongly support the notion that the top of the post-LMO cumulate pile was significantly denser than the bottom, consistent with a more recent numerical model (Elkins-Tanton et al. 2011), and thus prone to gravitational instability and cumulate overturn. This density difference is the result of increasing Fe contents of the minerals and melts as crystallization proceeded.

Evolution of experimentally determined residual LMO liquids (Fig. 2) show broad similarities with the Snyder et al. (1992) model, but there are important differences. The closest similarities are for MgO and Mg#, which show comparatively smooth decreases with increasing PCS. TiO_2 contents also show similar trends to those in the model, with a gradual increase until about 80 PCS, followed by a much sharper rate of increase and then an abrupt decline once ilmenite begins to crystallize. The modeled decrease in TiO_2 is steeper than the experimentally determined decreases. However, Ti is a major component in ilmenite and slight differences in ilmenite crystallization would control the Ti content in the small volume of remaining liquid, which could explain the differences between the models and experimental data.

In contrast, there are important mismatches between measured and modeled residual liquid compositions, particularly at high PCS. For CaO and FeO, the model predicts fairly sharp decreases in the last ~10% of solidification, whereas the experimental liquid compositions showed either stable or increasing abundances. In contrast to the Snyder et al. (1992) model, fractional crystallization experiments indicate that the FeO composition of the liquids continued to increase after ilmenite saturation. For Al_2O_3 and SiO_2, steep increases are predicted over the 90–100 PCS interval, but the experimental liquids showed sharp decreases

after peaking at ~85 PCS. These mismatches can be attributed to the stabilization of a silica phase in experimental results, which is not predicted by the models. These mismatches could also be attributed somewhat to the differences in ilmenite abundances between the modeled (~11% ilmenite) and experimentally determined systems (< 5%) (Lin et al. 2017b; Rapp and Draper 2018). Note that the experiments from Lin et al. (2017b) produced 12% ilmenite at PCS 96.4 for an anhydrous bulk composition; thus there is some experimental agreement with the Snyder et al. (1992) model regarding ilmenite abundance.

Residual liquids from the fully fractional experiments on LPUM and TWM became quite P-rich, with 2–4 wt. % P_2O_5; they also contained ~0.5–0.9 wt. % Na_2O and 0.1–0.2 wt. % K_2O (Rapp and Draper 2018). Trace element partitioning data from these and related studies (e.g., Rapp and Draper 2018; Dygert et al. 2020) suggest that these liquids would have KREEP-like REE patterns. These liquids coexisted with an evolved assemblage as described in the previous section and provide strong support for the hypothesis that KREEP was the product of protracted LMO crystallization and therefore represents the last liquid residuum of the magma ocean (Warren and Wasson 1979; Warren 1985).

The results of the LMO solidification experiments summarized here provide strong support for key features of the magma ocean model, highlight several avenues of potential experimental and theoretical research on LMO processes, and also raise new questions. In general, numerical models can benefit from these well-determined, internally consistent phase equilibria results for the bulk compositions used (Table 1). Inferences regarding post-LMO magmatism, such as the Mg- and alkali suites, can be expanded from the type presented by Elardo et al. (2011) now that LMO solidification has been much more fully simulated experimentally. Partition coefficients for a range of useful trace elements in key LMO phases (olivine, pyroxene, plagioclase, ilmenite) were reported in studies of fully fractional LMO crystallization with the LPUM composition (Rapp and Draper 2018) as well as in other studies by Van Kan Parker et al. (2011a,b), Sun and Liang (2013), Sun et al. (2017) and Dygert et al. (2013, 2014, 2020). Pressure–temperature conditions at which putative matches to lunar basalts are formed would enhance understanding of the thermal structure of the lunar interior. More comprehensive water-bearing LMO experiments than completed to date, starting from a basis of known anhydrous phase relations, can be designed to explore the still-widely-disparate range of possible interpretations for the water content of the Moon and its effect on lunar magmatic processes.

These experimental results indicate that fully fractional crystallization of the LMO would have produced a mono-mineralic olivine cumulate until > 50% crystallization. However, results of the two-stage crystallization experiments indicate that initial equilibrium crystallization is capable of stabilizing early Al-bearing orthopyroxene in addition to aluminous phases such as garnet or Cr-spinel. According to Rapp and Draper (2018), this early stabilization of Al-bearing phases during equilibrium crystallization would sequester sufficient aluminum from the starting LMO composition, reduce the amount of plagioclase crystallization, and thereby generate an overall thinner crust, similar in thickness to that estimated from GRAIL observations. However, the poorly-constrained Al content of the bulk Moon (Table 1) is another variable that can introduce uncertainty in predictions of early crystallization of Al-bearing phases and the resultant estimations of crust thickness. Lin et al. (2017b) and Charlier et al. (2018) suggest the discrepancy between crustal thickness estimates from GRAIL data and predicted by experimental results cannot be fully resolved even with a shallow magma ocean. Lin et al. (2019) suggested that water in the LMO could resolve this discrepancy. In all cases however, the precise accumulation rate of possible stable minerals contributing to a given primary cumulate pile are not fully constrained.

The likely compositions of KREEP-rich final LMO liquids have been established with experiments and models, but the processes that generate KREEP-rich lithologies and Ti-rich magmas remain elusive (e.g., potential hybridization and whether that hybridization took place

during passage through the crust or at the source of initial melting). Though the experiments indicate that that the very late-stage residual liquids of LMO solidification would have a KREEP-like composition, debate continues regarding the apparent concentration of KREEP in the PKT and whether KREEP exists as a globally distributed horizon (e.g., Elardo et al. 2020; Gross et al. 2020). A focus of future investigations should be to address this conundrum to establish the geographic extent of KREEP and the degree to which its distribution is consistent with magma ocean model predictions. Other future investigations could address potential processes in which LMO solidification and overturn occur contemporaneously (Boukaré et al. 2018). Constraining all these processes would enhance understanding of both the compositional and thermal structure of the lunar interior.

4. CONSTRAINTS ON LUNAR DIFFERENTIATION FROM PHYSIOCHEMICAL MODELING

New approaches for modeling primordial lunar differentiation have been developed to constrain the physiochemical processes that may have operated during and through the aftermath of solidification of the LMO. Over the past decade, modeling efforts have focused on establishing the existence, size, and composition of the lunar core, as well as defining the thermodynamics of a magma ocean, the physical behavior of crystal formation and segregation from a magma, and the effects of density and viscosity contrasts between lithologic units that result from magma ocean crystallization. These models have been developed upon spacecraft-based observations from the past decade and modern analysis of Apollo era seismograms, returned sample studies, and experimental studies of the solid phases that crystallize from a magma ocean and elemental distributions among phases. The outcomes of these models and the extent to which they reproduce physical observations of the Moon and its rocks provide a means to evaluate our current understanding of the magma ocean model and its fundamental predictions: an anorthosite crust; dense ilmenite-rich mantle regions; overturn and mixing of magma ocean crystallization products; and the surface expression of the incompatible- and heat-producing-element-enriched KREEP component.

4.1. Size and composition of the core

Several lines of evidence point towards the existence of a small (< 2.5 mass %) lunar core, including the identification of an ancient lunar magnetic field (e.g., Hood et al. 2001; Tsunakawa et al. 2010; Tikoo et al. 2014; Steenstra and van Westrenen 2017), the depletions of siderophile elements relative to the inferred building blocks of the Moon (Wänke et al. 1974; Steenstra and van Westrenen 2016), and geophysical observations (e.g., Garcia et al. 2011, 2012; Weber et al. 2011; Williams et al. 2001, 2014). Modern analyses of Apollo-era lunar seismograms find that the data are consistent with the current existence of a lunar core having a 330 ± 20 km radius, with a partially molten outer layer and a solid inner core with a radius of 240 ± 10 km (Weber et al. 2011). Recent results from the GRAIL mission provided additional constraints on the dimensions and thermal state of the lunar core (Williams et al. 2014), and suggest that the known density, moment of inertia, and Love number of the lunar core are matched with a fluid outer core with a radius of 200–380 km and/or a solid 0–280 km radius inner core. This range of possible sizes corresponds with a mass fraction of the combined inner and outer core of <1.5 % of the total Moon mass (Williams et al. 2014). This calculated mass percent is close to that derived from geochemical models based on a wide range of siderophile element depletions in the lunar mantle (Righter 2002; Rai and van Westrenen 2014; Steenstra et al. 2016). Based on mineral physics constraints and seismic travel times, Antonangeli et al. (2015) propose a radius of ~245–250 km for the inner core and a thickness of ~80–85 km for outer core, which are close to or within the range of independent constraints from GRAIL (Williams et al. 2014).

The composition of the lunar core should greatly affect its temporal evolution. For example, Laneuville et al. (2014) showed that the duration of a core dynamo is dependent on the liquidus temperature of the metallic alloy, and therefore its composition. The composition of the core also determines the type of crystallization and physical properties, including its mass and seismic velocities (Weber et al. 2011; Laneuville et al. 2014; Williams et al. 2014; Antonangeli et al. 2015). The current fluid state of the outer core suggests the presence of light element(s), which reduce the solidus of the outer core and sustain a prolonged (partially) fluid state. Compositional convection in the core, which may be required for a dynamo, also implies the presence of light elements. Light elements such as silicon, hydrogen, and oxygen are unlikely candidates to significantly partition into the lunar core, as they do not exhibit sufficiently siderophile behavior at the expected core formation conditions (Ricolleau et al. 2011), whereas sulfur and carbon show relatively strong siderophile behavior under lunar core formation conditions (Boujibar et al. 2014; Chi et al. 2014; Steenstra et al. 2017). Weber et al. (2011) proposed that the lunar core should contain < 6 wt. % S, based on reanalysis of Apollo-era seismograms and consideration of molten metal alloy densities and liquidus conditions. Sulfur can significantly reduce the bulk density, sound velocity, and liquidus temperature of the core (Hauck et al. 2006; Weber et al. 2011; Jing et al. 2014). More recent studies suggested a wide range of possible core S contents. For example, Zhang et al. (2013a) proposed from thermochemical models that 5–10 wt. % S is required, whereas Laneuville et al. (2014) suggested an initial S content of 7 ± 1 wt. %, or > 12 wt. % if the Moon never crystallized an inner core. From Fe–S equation of state measurements, Jing et al. (2014) proposed that the lunar core contains 4 ± 3 wt. % S.

The composition of the core can also be studied by considering siderophile element depletions in primitive lunar rocks, because the metal–silicate partitioning of these elements depends on metal composition (e.g., Righter 2002; Rai and van Westrenen 2014; Steenstra et al. 2016, 2017). Rai and van Westrenen (2014) showed that the depletions of slightly siderophile elements Cr and V in the bulk silicate Moon relative to the inferred lunar building blocks can be explained by a S-rich core, or alternatively, by super-liquidus temperatures during core formation in the Moon (Steenstra et al. 2016, 2020).

Extensive analyses of lunar primitive glasses provide better constraints on the abundance of S and C in the lunar interior (Bombardieri et al. 2005; Chen et al. 2015; Hauri et al. 2015). If the lunar core fully chemically equilibrated with the lunar mantle, which is suggested by the stepwise depletion of siderophile elements in primitive lunar rocks (e.g., Steenstra et al. 2016), the abundances of S and C in these rocks can be used to provide constraints on core composition (Righter et al. 2017; Steenstra et al. 2017). A FeS-rich core should then be reflected by high abundance of S in the bulk silicate Moon (BSM). Steenstra et al. (2017; Fig. 4) performed mass balance calculations using recently reported BSM estimates of S, C, and Ni to argue for a S-poor core (< 0.2 wt. % S), because the estimated BSM abundance of 75 ppm S is far too low to reflect equilibration with a FeS-rich core. This hypothesis was confirmed by the experimental work of Righter et al. (2017), which used experimental phase diagrams to indicate that the core is FeS-poor (< 0.5 wt. % S). Both studies advocated for the presence of some C in the lunar core. Steenstra et al. (2017) estimated the lunar core should contain 0.6– 4.8 wt. % C, based on the abundance of C in the lunar mantle (Wetzel et al. 2015). Righter et al. (2017) used an earlier, lower estimate of C in the mantle to suggest that the core contains 0.4 wt. % C. Both studies used the abundance of Ni in the mantle to derive an estimate of ~10–24 wt. % Ni in the core. Note that these estimates are a function of the light element budget of the core and the pressure of core–mantle equilibration, with the latter forming a clear link with magma ocean depths as discussed in the next section.

4.2. Depth of magma ocean

Estimates of the depth of the magma ocean are intertwined with models of silicate crystallization sequences, estimates of bulk silicate Moon compositions, and plagioclase-rich crust thickness estimated from GRAIL data, as well as the comparison of mare basalt and primitive lunar glass chemistry to the phase relationships of the predicted deep magma ocean cumulates (e.g., Warren 1985; Longhi 2006; Wieczorek et al. 2013; see discussion in preceding section). These approaches have not yielded a widely accepted or consensus value for the depth of the magma ocean. The metal–silicate partitioning of siderophile elements is dependent on pressure, temperature, redox conditions and composition (e.g., Righter 2003; Steenstra and van Westrenen 2017). Thus, observed depletions of siderophile elements in the lunar mantle, relative to the inferred building blocks of the Moon, can provide independent constraints on the pressure and temperature at which the lunar core equilibrated with the mantle, and thereby provide an estimate of the depth of the magma ocean. Righter (2002) proposed that the core and mantle equilibrated at relatively high pressure (5 GPa), based on consideration of the depletions in the lunar mantle (as estimated from lunar basalt concentrations) of Ni, Co, Mo, W, P, Ga, and Re, suggesting the Moon was largely to fully molten during its early evolution. These results were refined and confirmed by Rai and van Westrenen (2014), who suggested that lunar core–mantle equilibration occurred between 4–5 GPa within the mantle solidus–liquidus temperature range at these pressures. Key elements in this study were V and Cr, which can be sufficiently siderophile either in the presence of several wt. % S in the lunar core, or alternatively, at high *P–T* conditions. Steenstra et al. (2016, 2020) revisited this model using a wider range of 15 siderophile elements and confirmed the results of Rai and van Westrenen (2014) (Fig. 4). They found that the depletions of V and Cr can also be explained by super-liquidus temperatures during core-mantle equilibration, instead of a S-bearing lunar core. Given the recent constraints from abundances of indigenous sulfur in lunar samples (e.g., Chen et al. 2015; Hauri et al. 2015) and the likelihood that the lunar mantle is not sulfide saturated (e.g., Bombardieri et al.

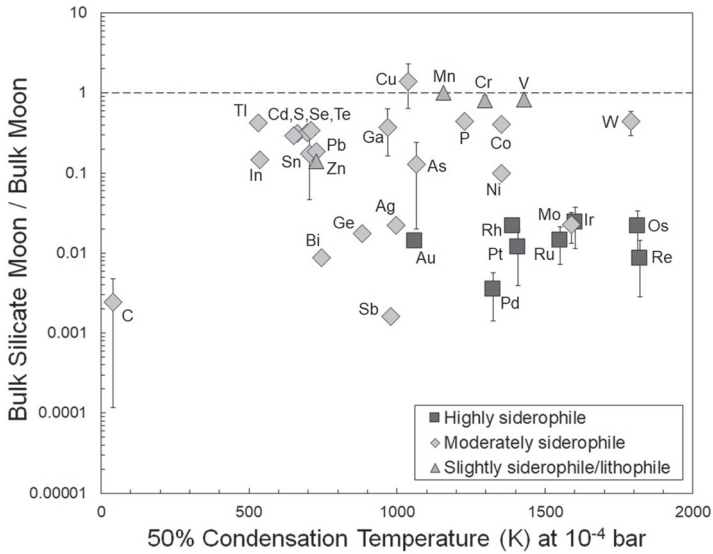

Figure 4. Siderophile elements in the bulk silicate Moon as a function of 50% condensation temperature at 10^{-4} bar (Lodders 2003) relative to the bulk Moon. Abundances of C, S, Mn, Zn, Ga, Ge, As, Se, Cd, In, Sn, Sb, Te, Tl, Pb, Bi and HSE in the bulk Moon are assumed to be equal to bulk silicate Earth (McDonough and Sun 1995; Fischer-Gödde et al. 2011).

2005; Ding et al. 2018; Day 2019), super-liquidus temperatures may be a more likely scenario. In a review of geochemical and geologic evidence, Pritchard and Stevenson (2000) determined at that time that the evidence did not preclude the formation of a molten Moon in a giant impact scenario, and this conclusion remains consistent with the predicted outcome of several recently proposed giant impact lunar formation scenarios (Canup 2012; Lock et al. 2016).

4.3. The physiochemistry of solidification on the Moon and crystal behavior

Solidification of the lunar magma ocean is expected to have initiated at high pressure, where the adiabat and solidus intersect (Walker et al. 1975; Solomatov 2000). However, because the potential temperature of the magma ocean was unlikely to be homogeneous azimuthally or radially, patterns of thermal convection would produce packages of magma ocean fluid with different potential temperatures and therefore crystallinities (see discussion in Elkins-Tanton 2012). The small pressure range of the Moon means that an adiabat in its well-mixed magma ocean would lie between its solidus and liquidus prior to the formation of a flotation crust (Tonks and Melosh 1990; Solomatov 2000), suggesting high crystal fractions and possible crystal networks.

Lunar sample suites, however, indicate fractional crystallization operated in the magma ocean, including flotation and segregation of plagioclase, unimpeded by high crystal fractions or crystal networks (Smith et al. 1970; Wood et al. 1970). Suckale et al. (2012a,b) undertook a detailed physical study of crystal flotation and found that crystal settling and flotation were probably possible throughout the entire solidification history of the LMO as long as crystal sizes were sufficiently large ($r > 1$ mm) and crystal fraction sufficiently low ($f < 13\%$). Plagioclase flotation in the later stages of magma ocean solidification therefore necessitates olivine and pyroxene crystal settling in the earlier stages of solidification, so that the crystal fraction in the magma ocean remained sufficiently low to allow formation of an anorthositic flotation crust (Suckale et al. 2012b). Formation of even an impure juvenile flotation crust would decrease the magma ocean solidification rate by many orders of magnitude (e.g., Elkins-Tanton et al. 2011), correspondingly increasing cumulate mineral grain sizes and reducing convection vigor, and thus promoting highly efficient crystal fractionation (e.g., Solomatov 2007; Dygert et al. 2017).

Experimental work summarized in the previous section explores compositional, and therefore density, variability produced by different bulk Moon compositions (Elardo et al. 2011; Lin et al. 2017a,b, 2019 ; Charlier et al. 2018; Rapp and Draper 2018). Density estimates of lunar mantle cumulates can be readily calculated using aforementioned LMO crystallization studies (see Li et al. 2019 for upper and lower bound estimates; Fig. 5). The bulk density of the late magma ocean cumulates depends in part on the efficiency of plagioclase flotation and segregation. The magma ocean saturated in ilmenite during the final stage of solidification (see below; e.g., Solomon and Longhi 1977); at this stage, ilmenite and Fe-rich clinopyroxene are expected to have precipitated and sunk into underlying cumulates and contributed to a layer of ilmenite-bearing cumulate (IBC) thicker than scenarios assuming perfect fractionation and instantaneous solidification of an LMO (Hess and Parmentier 1995, 2001; Li et al. 2019). The viscosity and density contrasts between the IBC and surrounding mantle control the rate and scale of IBC sinking and displacement of less dense cumulates in cumulate mantle overturn episodes (e.g., Parmentier et al. 2002; Dygert et al. 2016; Li et al. 2019; Yu et al. 2019; Zhao et al. 2019).

Recent experimental studies that constrain the viscosity of the lunar mantle focused on late magma ocean cumulate phases including Fe-rich olivine and ilmenite (e.g., Zhao et al. 2009; Till and Moskowitz 2013; Tasaka et al. 2015; Dygert et al. 2016). These and earlier work on Fe-rich clinopyroxene (Kollé and Blacic 1983) and magnesian olivine (e.g., Hirth and Kohlstedt 2004, and references therein) enable first-order predictions of lunar cumulate pile viscosity structure. At mantle-relevant temperatures and differential stresses, late magma ocean cumulates (ilmenite and Fe-rich clinopyroxene) would be one to more than three orders

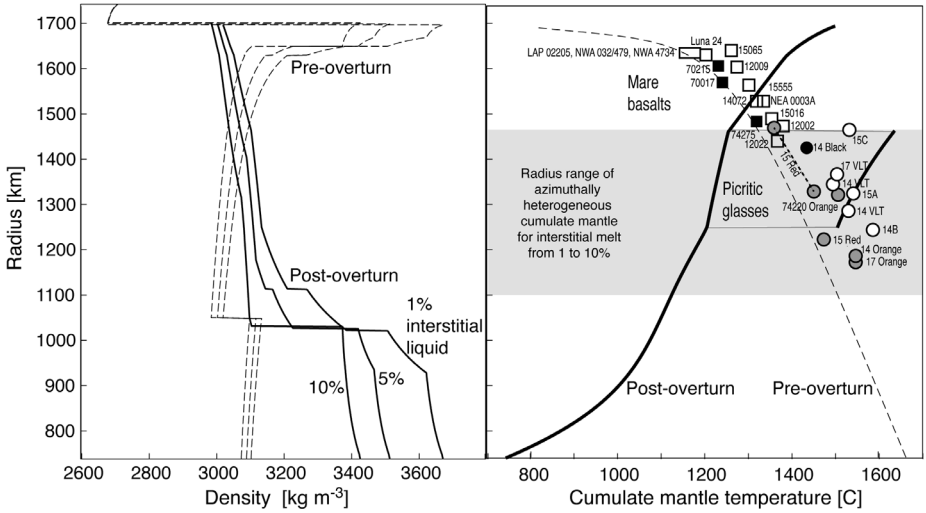

Figure 5. Cumulate mantle density and temperature profiles before and after solid-state overturn to gravitational stability. **Left**: Density of mantle mineral assemblages at reference pressure and solidus temperature; assumes mantle retains solidus temperature over period of solidification and carries temperature during overturn with only adiabatic adjustment and no conductive loss. Floated anorthosite lid is evident at radii greater than about 1700 km. **Right**: The pre-overturn temperature profile is the solidus adjusted for evolving bulk composition. After overturn the mantle is monotonic in density (**left**) but laterally heterogeneous in temperature and composition between ~1250 and 1450 km radius with 1 vol.% interstitial melt. **Horizontal guidelines** indicate radius ranges of compositional heterogeneity. The predicted radius range of heterogeneity in temperature and composition is based on the fractional model (Elkins-Tanton et al. 2011). The temperature profile would relax conductively on the timescale of hundreds of millions of years and also possibly be disrupted through convection. The pressures and temperatures of origin are shown for the mare basalts (**rectangles**) and picritic glasses (**circles**). **Black symbols** indicate high titanium content, while white symbols indicate low titanium. For references see Elkins-Tanton et al. (2004), with new additions here of 17 Orange and a new range for 15 Red, which depends upon fO_2, (Krawczynski and Grove, 2012), NEA 003A, LAP 02205, NWA 032/479, NWA 4734 (Elardo et al. 2015), and the 14 Orange (Brown and Grove 2015). [Reprinted from Earth and Planetary Science Letters, Vol. 304, Elkins-Tanton LT et al., The lunar magma ocean: Reconciling the solidification process with lunar petrology and geochronology, Figure 6, Copyright (2011), with permission from Elsevier.]

of magnitude weaker than early magma ocean cumulates (approximated by Fo_{90} olivine) (Fig. 6), and the viscosity contrasts are perhaps even larger depending on the temperature of the IBC and underlying mafic cumulates.

Olivine (and presumably pyroxene) rheology is highly sensitive to "water" (usually in the form of OH in crystal defects) and Fe content. At present, studies exploring the effect of Mg# on olivine rheology at mantle-relevant high pressures are few (e.g., Raterron et al. 2017). Low pressure and nominally dry experiments suggest that for olivine, the variation in viscosity between Fe and Mg-bearing end-members may be greater than three orders of magnitude (Zhao et al. 2009; Tasaka et al. 2015). Because the Mg# of the magma ocean cumulates likely decreased dramatically in the last few tens of percent crystallization (e.g., Snyder et al. 1992; Elkins-Tanton et al. 2011; Lin et al. 2017b), it is reasonable to expect that (excluding plagioclase) the last silicate phases to crystallize were more similar to ilmenite in viscosity than to the early cumulates.

Formation and overturn of the IBC would produce a hybridized mantle composed of mixtures of late- and early-formed cumulates. Strain partitioning among minerals in multiphase aggregates determines effective aggregate rheologies. Heterogeneous strain

partitioning is particularly important in rocks composed of relatively strong and weak phases such as ilmenite and olivine (e.g., Huet et al. 2014; Dygert et al. 2016; Tokle et al. 2017). In most cases, effective viscosities of multiphase aggregates fall between those of the constituent minerals (see Dimanov and Dresen 2005, Huet et al. 2014, and Dygert et al. 2016 for a summary of some relevant mixing laws). Experiments conducted on halite–calcite aggregates suggest that at high strains relevant to mantle convection, aggregate rheologies approach the rheology of the weakest phase, even at weak phase fractions as low as 10 volume percent (Jordan 1987). Because the wavelength or scale of cumulate overturn depend on viscosity (see below), reducing the uncertainty in predictions of multiphase aggregate viscosities is of primary importance for understanding the scale of cumulate mantle overturn and subsequent lunar mantle convection patterns.

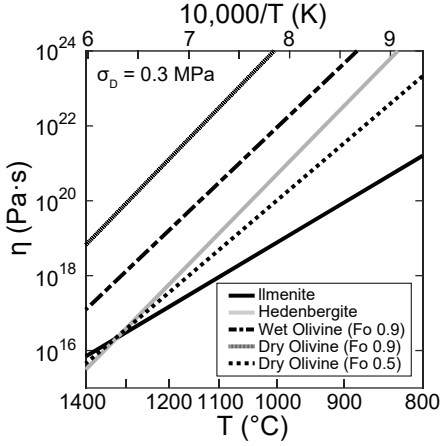

Figure 6. Viscosities of minerals relevant to the Moon calculated using experimentally parameterized single phase flow laws at a differential stress of 0.3 MPa (Kollé and Blacic 1983; Hirth and Kohlstedt 2004; Tasaka et al. 2015; Dygert et al. 2016). Note the relatively high viscosity of dry olivine (which may approximate the rheology of early magma ocean cumulates) compared to viscosities of late magma ocean cumulates (ilmenite, hedenbergite, and Fe-rich olivine). Viscosity of wet olivine is calculated assuming 1000 H/10^6 Si.

4.4. What overturned and what was the resulting compositional and thermal structure?

The expected density and viscosity structure of the lunar cumulate pile make overturn highly likely. Overturn would necessarily produce mixtures of late- and early-formed magma ocean cumulates ("hybridized" mantle sources) that, when melted, would form basalts compositionally similar to lunar picritic glasses (e.g., Papike et al. 1998; Thacker et al. 2009; Brown and Grove 2015). Overturn is not expected to produce a mineral-scale mixture, but rather radial layering, or, in the case of differently composed cumulates with the same density, azimuthally heterogeneous layers with compositional differences on the length scale of the wavelength of sinking dense cumulates (Elkins-Tanton et al. 2011).

An important feature of Ti-rich lunar basalts is their spatial confinement to the Procellarum KREEP terrane on the nearside (e.g., Lucey et al. 1998; Giguere et al. 2000; Sato et al. 2017). Several models investigated whether this confinement may have an overturn-related dynamic origin. Hemispheric, spherical harmonic degree-one overturn could concentrate hybridized basalt sources beneath the lunar nearside (Jolliff et al. 2000; Parmentier et al. 2002; Li et al. 2019). The thermal and compositional anomaly produced by a degree-one downwelling (or upwelling) structure, characterized by a single region of downwelling or upwelling, could also sufficiently perturb the Moon's moment of inertia to drive true polar wander, the existence of which has been inferred from spatial distributions of ice deposits in shadowed lunar craters (Siegler et al. 2017).

The wavelength, or scale, of lunar cumulate mantle overturn is controlled by the viscosities of the IBC and underlying cumulates, as well as the thickness of the IBC layer (Whitehead 1988; Hess and Parmentier 1995). Thick and low-viscosity IBC layers promote

long wavelength instabilities. Parmentier et al. (2002) found that when the viscosity contrast between the IBC and underlying cumulates is 10^4, degree-one (hemispheric) downwelling may occur. A large viscosity contrast between late and early cumulates is supported by single-phase flow laws (Fig. 6). However, to form degree-one downwelling instabilities, additional IBC viscosity reduction may be required, possibly by partial melting and/or high IBC water contents (e.g., Hirth and Kohlstedt 2004; Scott and Kohlstedt 2006).

Like degree-one downwelling, degree-one hemispheric upwelling of previously overturned cumulates could have resulted in a hemispheric concentration of IBC beneath the lunar nearside, for example, broadly coincident with the distribution of mare basalts (Zhong et al. 2000; Zhang et al. 2013a,b). Because of the high intrinsic density of the IBC, overturned IBC must be heated sufficiently to thermally expand and become buoyant, thereby forming upwelling diapirs. Zhang (2013a) found that in cases where the viscosity of the overturned IBC is low, vigorous convection in the IBC layer efficiently dissipates heat into the overlying ilmenite-free mantle and the IBC remains negatively buoyant. Formation of a degree-one upwelling instability requires an IBC viscosity greater than that of the ilmenite-free mantle (Zhong et al. 2000; Zhang et al. 2013a), which is not experimentally supported (Fig. 6). Numerical simulations suggest that upwelling diapirs that do develop after cumulate mantle overturn are likely to be of shorter wavelength (Zhang et al. 2017). Such upwelling diapirs may be critical for mixing IBC back into the overlying mantle and forming lunar basalt source regions at depths consistent with multiple-saturation experiments.

The preceding analysis suggests that cumulate overturn should have occurred at some scale, delivering IBC to the deep lunar interior (e.g., Hess and Parmentier 1995; de Vries et al. 2010; Li et al. 2019; Yu et al. 2019; Zhao et al. 2019). Very low viscosity IBC would have been highly stable around the core throughout geologic time (Zhang et al. 2013a; Dygert et al. 2016). Several lines of evidence support a layer of hot, partially molten IBC around the lunar core at the present day. Reinterpretation of seismic reflection data led Weber et al. (2011) to suggest a partially molten layer around a liquid outer core and solid inner core, and several authors (e.g., Van Kan Parker et al. 2012, Vander Kaaden et al. 2015) showed that Ti-rich partial melts at this depth would be negatively or neutrally buoyant. Studies investigating tidal dissipation argued for a low viscosity region around the lunar core (e.g., Harada et al. 2014, 2016; Khan et al. 2014; Williams and Boggs 2015). Such a layer coincides with an inferred seismically attenuating layer through which no farside moonquakes have been observed (e.g., Wieczorek 2009). Matsuyama et al. (2016) found that if a layer around the lunar core is present, it is most likely a high-density feature ($\rho \sim 4$ g/cc), consistent with an IBC-rich composition. A stable, heat producing element-rich IBC layer around the core would have prevented effective cooling of the core throughout geologic time, affecting the efficiency of a convection-driven core dynamo (Zhang et al. 2013a). Alternative mechanisms for driving a dynamo may be required (e.g., Weiss and Tikoo 2014; see also Wieczorek et al. 2023, this volume).

A fractional solidification model for the Moon predicts that some of the deepest, warmest materials that rise and melt adiabatically during overturn would have a high Mg#, from ~80 to 90. The crustal rocks of the Mg-suite exhibit this signature of elevated Mg#. Anorthite contents of plagioclase from Mg-suite samples are positively correlated with the Mg# of coexisting orthopyroxenes (e.g., Shearer et al. 2015). These characteristics are petrologically consistent with production of the Mg-suite parental magmas through melting of magnesian mantle cumulates during cumulate overturn (see Shearer et al. 2023, this volume).

4.5. Duration of magma ocean crystallization and timing of cumulate overturn

Solidification of a lunar magma ocean that is convecting and has a free surface would possibly be as rapid as 1 to 10 k.y. (e.g., Zahnle et al. 1988; Elkins-Tanton 2008; Elkins-Tanton et al. 2011). Once a solid conductive lid had formed on the magma ocean, heat flux would

be reduced by many orders of magnitude, and thus cooling and solidification times would be lengthened proportionately. Calculated using only radiative cooling, the lunar magma ocean would cool to 95–99% solid in 100–200 m.y. if it maintained a quench crust throughout solidification (Solomon and Longhi 1977) or 10 to 20 m.y. in an alternative endmember scenario where it cools as a convecting body beneath a free liquid surface until plagioclase saturates and forms a flotation crust (Elkins-Tanton et al. 2011). The addition of tidal heating and convection has a profound effect on solidification. The solid anorthosite lid would flex and heat efficiently under the gravitational effects of the still-nearby Earth; additional heat would be added by partial melting of deep cumulates undergoing convection, lengthening the time of solidification of the magma ocean to up to 200 m.y. (Meyer et al. 2010; Chen and Nimmo 2016; Maurice et al. 2020).

The relative timing of cumulate overturn is controlled by the interplay of magma ocean crystallization rate, and the cumulate viscosity (discussed above) and thermal structure. A geodynamical model of the permissible range of these parameters as modeled for the LMO allow for early as well as late overturn (Boukaré et al. 2018). In the early overturn scenario, cumulate overturn prior to ilmenite saturation is driven by thermal convection rather than cumulate density contrasts, and results in a well-mixed mantle (Boukaré et al. 2018), which is expected to overturn again after solidification of late-formed ilmenite-bearing magma ocean cumulates. In late overturn scenarios, in which overturn occurs after ilmenite saturation, the timescale of overturn and completeness of mixing depend on the viscosity of the ilmenite-bearing cumulate, which in turn has a strong dependence on the presence of an insulating crust as well as radiogenic heat production from proximal partially molten urKREEP (Yu et al. 2019; Zhao et al. 2019).

On the low-gravity Moon during the first 80% or so of solidification, model-based times to initiation of density-driven overturn range from tens of thousands to millions of years (Hess and Parmentier 1995; Elkins-Tanton et al. 2011). After ilmenite saturation, the time to density-driven initiation of overturn is thousands of years, and therefore overturn is likely to initiate before solidification is complete (Hess and Parmentier 1995; Elkins-Tanton et al. 2011; Boukaré et al. 2018). In this model scenario, large-scale overturn events are likely to have happened at most 5 to 50 m.y. after the first anorthosite flotation. If indeed the Mg-suite crustal intrusive rocks were formed by overturn, then anorthosite flotation initiated at most 5 to 50 m.y. before the crystallization ages of Mg-suite samples. The following section discusses the chronological constraints on the absolute and relative timing on FAS and Mg-suite magmatism.

5. CHRONOLOGY OF LUNAR DIFFERENTIATION

Recent investigations have sought to define the timing of lunar differentiation using two complementary approaches. First, isotopic analyses of individual lunar samples are used to define the crystallization ages of the materials that are predicted by the magma ocean model to be the oldest on the Moon. These investigations have focused on rocks and minerals from the Apollo sample collection, including samples for which ages had not yet been determined, as well as rocks for which ages had been previously measured. In the second approach, novel and well-established techniques alike have been applied to suites of lunar samples to define isotopic model ages of magmatic events associated with solidification of the LMO. These investigations establish the timing of large-scale or global events that are defined by geochemical differentiation of the Moon, and by formation of geochemical reservoirs predicted to result from solidification of the LMO. Although neither of these approaches are conceptually new, their use over the past decade-and-a-half has been accompanied by technical advances in analytical methods and instrumentation, as well as a more thorough understanding of the effects of cosmic neutron irradiation on isotopic compositions of lunar rocks and minerals, which enable some chronological measurements to be performed with a higher fidelity than was possible in preceding decades.

5.1. Age measurements of individual samples

The apparent timing and duration of FAS and Mg-suite magmatism defines a long-standing conundrum in the chronology of lunar differentiation and ancient lunar crustal magmatism. In the widely accepted standard magma ocean model, FAS samples represent direct crystallization products of the LMO (e.g., Smith et al. 1970). Therefore, FAS magmatism is predicted to have occurred over a relatively short time frame, and crystallization ages of FAS samples are thought to record the time at which the magma ocean reached plagioclase saturation after about 70–80 % LMO solidification (Fig. 3). In turn, Mg-suite magmatism, which bears a KREEP compositional signature in the Apollo samples (but not necessarily in other samples; see Gross et al. 2020), is predicted to post-date urKREEP formation during the final stages of magma ocean solidification. As urKREEP is the final crystallization product predicted to form in most LMO solidification models, urKREEP formation is interpreted to mark the end of primary differentiation of the Moon through LMO solidification in most of the studies discussed below. However, these chronological relationships are not uniformly observed in analyzed samples. Rather, ages determined for FAS samples span nearly 270 m.y., and the range of ages determined for FAS samples overlaps the range of ages determined for Mg-suite samples (Fig. 7). A further complication in the interpretation of these age measurements is the issue that, in some cases, replicate age measurements performed on individual samples do not yield reproducible results; in all cases, replicate age measurements have yielded or reproduced younger, rather than older, ages (Fig. 7). This observation reflects a combination of issues including: 1) many samples are small, nearly monomineralic, and have low abundances of the isotopes used to date them making age determinations technically difficult, 2) protracted bombardment of the lunar surface is expected to have disturbed or fully reset the isotope systematics of many ancient lunar rocks (Gaffney et al. 2011; Borg et al. 2015), 3) slow cooling of lower-crustal intrusive rocks results in substantial time gaps between emplacement of the plutons and the termination of parent-daughter isotope diffusion and closure of the chronometer (McCallum et al. 2006; Borg et al. 2017), and 4) varying methods used to correct the Sm–Nd chronometer for the capture of thermal neutrons on the lunar surface (Gaffney and Borg 2014; Borg et al. 2015). In the effort to resolve these long-standing issues surrounding the timing and duration of lunar differentiation, much of the chronology research undertaken over the past decade-and-a-half has focused on developing new analytical methods and approaches that take advantage of modern high-precision mass spectrometry and ultra-low blank Pb isotopic analyses, and using these methods to measure internal mineral isochron ages and Pb–Pb ages of mineral separates for samples in the Apollo sample collections.

Recent efforts to establish a more accurately defined age range for FAS magmatism have produced a 140 m.y. range of ages for FAS samples, compared to a range of 270 m.y. determined with earlier studies (Nyquist et al. 2006; Borg et al. 2011; Marks et al. 2019; Sio et al. 2020). It is particularly challenging to determine the crystallization ages of FAS materials because they contain very low abundances of mafic minerals and low concentrations of REE, and many FAS samples are breccias, representing several FAS lithologies. Reanalysis of one sample, 60025, yielded a highly precise age of 4360 ± 3 Ma that is defined by three separate isotope chronometers: ^{147}Sm–^{143}Nd, ^{142}Nd–^{143}Nd and ^{206}Pb–^{207}Pb isotope systems (Borg et al. 2011). This age is younger than the previously measured age of 4440 ± 20 Ma (Carlson and Lugmair 1988). Other FAS samples recently dated include 60016 (4302 ± 28 Ma, 4296 $^{+39}/_{-53}$ Ma, 4275 ± 38 Ma, and 4311 ± 31 Ma; Marks et al. 2019), 62237 (4350 ± 73 Ma; Sio et al. 2020), and Yamato 86032 (4438 ± 34 Ma; Nyquist et al. 2006). These age determinations together define a time span of 140 m.y. and thus under the simple assumption that these represent crystallization rather than recrystallization or alteration ages, appear to represent a long duration for FAS magmatism.

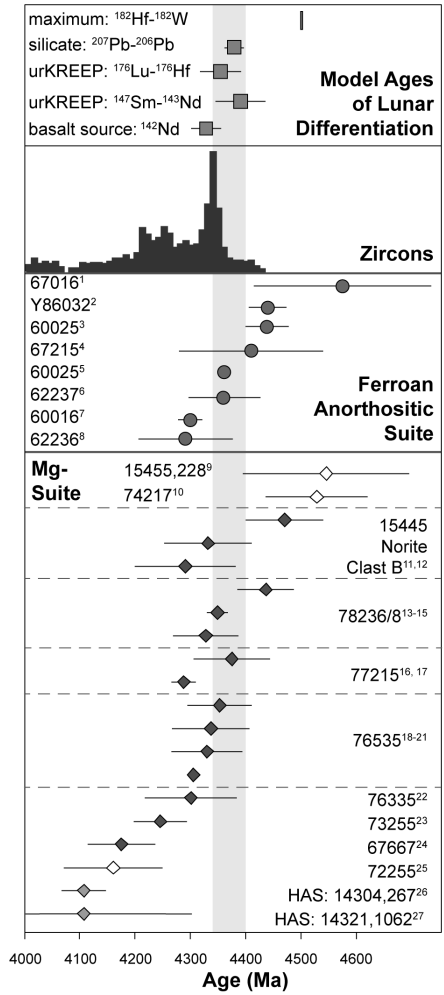

Figure 7. Maximum age of lunar differentiation is constrained by ^{182}W analyses by Kruijer and Kleine (2017) and Touboul et al. (2015). Silicate differentiation ^{207}Pb-^{206}Pb model age is from Snape et al. (2016). Model ages for urKREEP formation are from Gaffney and Borg (2014), and the average of these is represented by vertical gray box. ^{142}Nd model age for mare basalt source formation is calculated using ^{146}Sm t½ = 103 My (Friedman et al. 1966; Meissner et al. 1987), and is the average of ages determined by Boyet and Carlson (2007), Brandon et al. (2009), McLeod et al. (2014) and Nyquist et al. (1995). Ages determined for zircons are represented in a histogram with 10 m.y. bins of individual analyses published by: Barboni et al. (2017), Crow et al. (2017), Grange et al. (2009, 2011, 2013a, 2013b), Hopkins and Mojzsis (2015), Meyer et al. (1996), Nemchin et al. (2006, 2008, 2009a, 2009b, 2017), Pidgeon et al. (2007), Taylor et al. (2009). Isochron ages for individual samples are recalculated from published results using a common calculation method (Isoplot 4.15), and data that have been normalized to common standard values (La Jolla $^{143}Nd/^{144}Nd$ = 0.511845; NBS 987 $^{87}Sr/^{86}Sr$ = 0.710245), following the approach detailed by Borg et al. (2014). Rb–Sr isochron results (white diamond symbols) are presented only when the age of the sample has not been determined using a Sm–Nd isochron. 1: Alibert et al. (1994), 2: Nyquist et al. (2006), 3: Carlson and Lugmair (1988), 4: Norman et al. (2003), 5: Borg et al. (2011), 6: Sio et al. (2020); 7: Marks et al. (2014), 8: Borg et al. (1999), 9, 11: Shih et al. (1993), 10: Papanastassiou and Wasserburg (1975), 12: Gaffney et al. (2015), 13: Nyquist et al. (1981), 14: Edmunson et al. (2009), 15, 23: Carlson and Lugmair (1981a), 16: Nakamura et al. (1976), 17: Carlson et al. (2014), 18: Lugmair et al. (1976), 19: Nyquist et al. (2012), 20: Premo and Tatsumoto (1992), 21: Borg et al. (2017), 22: Edmunson et al. (2007), 24: Carlson and Lugmair (1981b), 25: Compston et al. (1975), 26: Snyder et al. (1995), 27: Shih et al. (1985).

The time of onset of Mg-suite magmatism defines the youngest possible age for primary lunar differentiation during LMO solidification. However, internal mineral isochron ages measured for Mg-suite samples in earlier studies span a wide range of ages and do not clearly delimit the onset of Mg-suite magmatism. This may be expected given the potential for extended heating of the lower crust or upper mantle by decay of radionuclides concentrated in urKREEP (e.g., Hess and Parmentier 2001), and the consequent delayed closure of radiometric systems. Replicate isochron analyses have been completed for several Mg-suite samples. For some samples, such as troctolite 76535, replicate Sm–Nd age measurements yield reproducible ages between 4330 ± 64 Ma and 4253 ± 58 Ma, indicating that the measured ages likely represent the time at which the sample cooled below the closure temperature of the isotope system used to measure the internal isochrons (Fig. 7). In other cases, ages do not agree. In the case of 15445 norite clast B, discordant Sm–Nd isochron ages of 4291 ± 91 Ma and 4470 ± 70 Ma were determined for two separate pieces of this sample (Shih et al. 1993). Recent reanalysis of this sample found an intermediate crystallization age, 4332 ± 79 Ma (Gaffney et al. 2015). Most recent analyses of other Mg-suite samples similarly yield crystallization ages around 4300 to 4350 Ma (Fig. 7), suggesting that the oldest ages record the onset of Mg-suite magmatism, and that this time can be considered the youngest age limit on primary lunar differentiation.

Zircon crystals constitute a third population of samples for which crystallization ages may constrain the timing of lunar differentiation. Although zircons have long been recognized as robust recorders of age information, a key challenge in the interpretation of lunar zircon ages lies in the fact that the majority of lunar zircons that have been dated are detrital or inherited, and thus it is not always possible to establish their original petrogenetic and geologic context. Zircons crystallize from magmas with high Zr concentrations (> 5000 ppm) and therefore are primarily associated with evolved and/or KREEP-rich magmatism, although extreme crystallization (> 99.9%) of a basaltic magma can also produce zircon saturation. If zircons are direct crystallization products of the lunar magma ocean, then they are extremely late-stage; the majority of lunar zircons are more likely to have crystallized during secondary magmatism or impact-related processes. In either case, crystallization ages of zircons place a younger age limit on the timing of lunar differentiation. The population of zircon ages, determined by in situ SIMS Pb–Pb and U–Pb analyses, defines a dominant peak around 4350 Ma (Fig. 7). This population has a tail that extends to slightly older ages, with a maximum age of 4417 ± 6 Ma which has been interpreted to represent the youngest age limit for lunar differentiation (Nemchin et al. 2009a).

The analytical efforts undertaken over the past decade to define the chronology of lunar differentiation from direct crystallization age measurements of samples, either through internal mineral isochrons of FAS and Mg-suite samples, or through in-situ SIMS analyses of zircons, have largely produced a population of sample ages around 4.35 Ga. In the effort to evaluate and intercompare these ages in the context of age measurements completed over the preceding several decades, Borg et al. (2015) recalculated internal isochron ages for FAS and Mg-suite samples using analytical data that were normalized to common isotopic standards, and using a common isochron-fitting algorithm. They then defined a set of criteria with which to evaluate the 'reliability' of internal mineral isochron ages. These criteria include: 1) concordant ages are determined with more than one isotope system, 2) isotope ratio measurements used to define isochrons exhibit limited scatter, 3) initial isotopic compositions defined by isochrons are consistent with the sample's petrogenesis, 4) ages are defined by isotope systems that are resistant to disturbance, and 5) REE concentrations determined by isotope dilution analyses of mineral separates are consistent with independent in situ analyses (Borg et al. 2015). When these criteria are applied to the entire range of isochrons determined for FAS and Mg-suite samples, the ages that have the highest reliability index define a relatively narrow range between 4.34 and 4.37 Ga. If the FAS samples constrain the timing of primary differentiation during the latter stage of LMO solidification, and Mg-suite samples are taken to constrain the timing of secondary (overturn-related) lunar differentiation, then the near-concordance of the most

reliable FAS and Mg-suite ages indicates that these differentiation events were late, quick, and essentially coincident. Although these ages do not in and of themselves constrain the age of the Moon, they do require a major magmatic event around 4.34–4.37 Ga that produced the rock suites and sources canonically attributed to magma ocean solidification.

The ages recorded by internal mineral isochrons represent the time at which the sample cooled below the closure temperature for the relevant isotope system. Modeling of the thermal state of the early Moon indicates that tidal heating of the anorthositic crustal lid may have retained anorthosites at temperatures above the isochron closure temperatures for as long as 200 m.y., or, impact-related excavation of a deeply-emplaced plutonic rock may record the excavation age rather than the emplacement age (Marks et al. 2019). Although extended cooling would result in internal isochrons in plutonic rocks that might record ages substantially younger than the time of pluton emplacement, slow cooling is identifiable through examination of mineral textures and compositions. Such observations of FAS samples 60025 and 67075 have been interpreted to record cooling in a plutonic setting, rather than extended subsolidus reequilibration (McCallum and O'Brien 1996). Furthermore, in the case of extended cooling, the initial Nd isotopic composition would reflect the bulk Nd isotopic composition of the anorthosite at the time of re-equilibration, not the Nd isotopic composition of the magma ocean source from which the anorthosite crystallized; observations of near-chondritic initial Nd isotopic compositions in FAS samples are not consistent with extended cooling of these samples (Sio et al. 2020). Mg-suite troctolite 76535 is one notable exception; the phase relationships, mineral compositions and textures of this sample show that this sample experienced subsolidus recrystallization and/or metasomatism (McCallum and Schwartz 2001; Elardo et al. 2012). Extended heating in the crust, accompanied by metasomatism by an infiltrating melt, maintained equilibrium for an extended duration after pluton emplacement, and the ages recorded by these different isotope chronometers represent the time at which the rock cooled below the closure temperature for each isotope pair (Borg et al. 2017). In 76535, ages are correlated with the closure temperature of the isotope system, and range from a plagioclase Pb–Pb age of 4226 ± 35 Ma (Premo and Tatsumoto 1992; closure temperature = 624 ± 9 ˚C), to a Sm–Nd isochron age of 4307 ± 11 Ma (Borg et al. 2017; closure temperature = 825 ± 15 ˚C). In this case, the oldest age places a younger limit on the crystallization age of the sample; extrapolation of the cooling rate to the solidus temperature requires additional constraints on the high-temperature history of the sample (Hammer et al. 2017).

5.2. Model ages of lunar differentiation

The now-extinct ^{182}Hf–^{182}W isotope system constrains the timing of Moon formation and differentiation. Core formation in the Moon or Earth causes significant fractionation of siderophile W from lithophile Hf; a lesser degree of Hf–W fractionation results from silicate differentiation. If these processes occur while ^{182}Hf is extant ($t_{½}$ = 8.9 My), then decay of ^{182}Hf to ^{182}W will result in variable ^{182}W/^{184}W ratios among lunar rock types, and different ^{182}W/^{184}W ratios between the silicate Moon and Earth. Work with these isotope systems in the mid 2000s revealed that the silicate Moon and silicate Earth had indistinguishable ^{182}W/^{184}W and that different lunar rock types were homogeneous (Touboul et al. 2007) or had only slight variability (Kleine et al. 2005) in measured ^{182}W/^{184}W compositions, indicating that the Moon formed about 60 m.y. or more after the start of the solar system. More recently, increased precision in ^{182}W/^{184}W isotopic analyses and more detailed models for correction of neutron irradiation effects on W isotopic composition have produced high-resolution results for a wide range of lunar rock types. Studies by Kruijer et al. (2015), Touboul et al. (2015) and Kruijer and Kleine (2017) showed that, although the rock types and their magma sources are characterized by highly variable W/Hf ratios, the W isotopic compositions of these rock types are uniform, indicating that lunar differentiation post-dated extinction of ^{182}Hf about 70 m.y. after CAI formation, for an oldest possible age of lunar differentiation of about 4.50 Ga.

The Pb isotope systematics of solar system materials were one of the first datasets used to establish radiometric constraints on the age of the solar system and its bodies, and analytical advances continue to support chronological advances using the ^{206}Pb–^{207}Pb system. Lead isotope model ages take advantage of the fact that two isotopes of U decay to two isotopes of Pb (^{235}U–^{207}Pb and ^{238}U–^{206}Pb), with substantially different parent isotope half-lives, thereby enabling chronometric information to be determined solely from isotopic analysis of Pb. The Pb isotopic evolution of the Earth and Moon is controlled by the U/Pb ratio of the solar system, and planet formation or differentiation events that cause U–Pb fractionation within bodies. Two recent investigations (Connelly and Bizzarro 2016; Snape et al. 2016) used Pb isotopic evolution models to constrain the timing of formation and differentiation of the Moon. In one, SIMS isotopic analyses of lunar mare basalts, KREEP-basalts and a breccia were used to define the initial Pb isotopic compositions of lunar magma sources. The Pb isotopic evolution models for these initial compositions require at least two stages of isotopic ingrowth, with the second stage defined by formation of the FAS and urKREEP concurrently at 4376 ± 18 Ma (Snape et al. 2016). The timing of the first stage, interpreted as formation of the Moon, is less well constrained, and is dependent on the U/Pb ratio assumed for the bulk Moon. A high μ (μ = $^{238}U/^{204}Pb$) value for the bulk Moon (1063 ± 184) is consistent with a young formation age of 4425 Ma, whereas a lower bulk Moon μ value (274 ± 50) is consistent with an older formation age coincident with the age of the solar system (4567 Ma) (Snape et al. 2016). Connelly and Bizzarro (2016) applied a very different approach, in which they inferred the timing of the giant impact and Moon formation from model Pb isotopic evolution of the Earth. The latter is consistent with Pb loss from bulk silicate Earth around 4426–4417 Ma; the authors interpret this Pb-loss event to be the Giant Impact and subsequent formation of the Moon. This scenario is consistent with the conclusions of Snape et al. (2016) if the bulk silicate Moon has a high μ-value of about 1000.

Further evaluation of these Pb isotope evolution models requires a more detailed assessment of the mechanisms for U–Pb fractionation during the Moon-forming event and also during lunar differentiation. Lead is a volatile element, but the extent to which Pb may be lost from the Earth-Moon system and the bulk Moon separately during the Giant Impact and condensation of the Moon is not well constrained. These models require a large degree of Pb-loss from bulk silicate Earth, but an even larger extent of Pb loss from the bulk Moon (Snape et al. 2016). Furthermore, the Pb isotopic evolution of the different lunar geochemical reservoirs formed during differentiation (FAN, mare basalt sources, urKREEP) likewise requires extensive U–Pb fractionation among these reservoirs (Tera and Wasserburg 1974). Although plagioclase crystallization may accomplish this fractionation in part, more comprehensive modeling requires determining a set of U and Pb partition coefficients relevant to these specific processes.

Model ages for the formation of urKREEP and the mare basalt sources may be interpreted to represent the time at which these geochemical reservoirs were last in isotopic equilibrium with the bulk silicate Moon, and in that context, constrain the time at which they formed during lunar differentiation through solidification of the LMO. The ages and initial isotopic compositions of KREEP-rich samples define the $^{143}Nd/^{144}Nd$ and $^{176}Hf/^{177}Hf$ growth curves of the urKREEP source. The slope of this growth curve defines the $^{147}Sm/^{144}Nd$ and $^{176}Lu/^{177}Hf$ of urKREEP, and the intersection of the urKREEP growth curve with the curve depicting evolution of a chondritic reservoir is interpreted as the time at which urKREEP differentiated from the chondritic silicate Moon. This calculation has been completed in several studies (e.g., Carlson and Lugmair 1979; Nyquist and Shih 1992), using the Sm–Nd internal isochron ages and initial Nd isotopic compositions available at the time. More recently, Gaffney and Borg (2014) included only Sm–Nd analytical data for isochrons that were determined to be the most reliable using the five criteria described above and calculated a Sm–Nd model age

for urKREEP formation of 4389 ± 45 Ma. This age represents the time at which the urKREEP reservoir separated from the bulk Moon and began to isotopically evolve independently. This approach has also been used for initial Hf isotopic compositions of samples. As with the W isotopic system, the Hf isotopic system is affected by neutron irradiation, so measured isotopic compositions must be corrected for the surface effects of cosmic ray interactions (Sprung et al. 2013; Gaffney and Borg 2014). Hafnium isotopic compositions of KREEP-rich Mg-suite and KREEP basalt samples, corrected for neutron irradiation effects and assuming a chondritic source, define a model age for urKREEP formation of 4353 ± 37 Ma (Gaffney and Borg 2014). Similarly, Sprung et al. (2013) used KREEP-rich breccias rather than KREEP-rich igneous rocks and obtained a concordant, though slightly older, age of 4402 ± 23 Ma. Note that the difference in age may reflect the poorly constrained crystallization ages derived from the breccia samples used in the Sprung et al. (2013) investigation. Recently, Maurice et al. (2020) developed a physical model that predicted that magma ocean solidification occurred over an extended duration of up to 200 m.y., depending on a range of assumed physical parameters. They calculated a range of $^{143}Nd/^{144}Nd$ and $^{176}Hf/^{177}Hf$ evolution trajectories of the residual mama ocean liquid over this time interval, with the ultimate values representing the initial isotopic compositions of urKREEP. Using the range of calculated sub-chondritic initial isotopic compositions (as opposed to the chondritic initial isotopic compositions assumed in the studies described above), Maurice et al. (2020) used a Monte Carlo model to fit residual magma ocean liquid and urKREEP evolution curves to the $^{143}Nd/^{144}Nd$ and $^{176}Hf/^{177}Hf$ compositions of KREEP-rich rocks measured by Gaffney and Borg (2014), to calculate urKREEP formation ages of 4220 to 4270 Ma. Notably, these model urKREEP formation ages are younger than the crystallization ages of most Mg-suite samples, contrasting with most petrogenetic models that predict that Mg-suite magmatism postdates urKREEP formation (e.g., Shearer et al. 2015).

Isotopic compositions of zircons have also been used to calculate urKREEP model ages. Taylor et al. (2009) used the Hf isotopic compositions of a population of zircons to define an urKREEP model age of 4478 ± 92 Ma. However, these Hf isotopic compositions were not corrected for the effects of neutron irradiation, which has since been recognized to affect Hf isotopic measurements. A modified approach was used more recently by Barboni et al. (2017), who applied corrections for neutron capture to the measured Hf isotopic compositions of zircon crystals to calculate a model age. Whereas Taylor et al. (2009) used the full population of zircon analyses to define a probability distribution for the model age, Barboni et al. (2017) calculated individual model ages for each zircon crystal and assumed that the four oldest calculated model ages define the urKREEP model age of 4510 ± 10 Ma. These model ages were calculated assuming the extreme yet unrealistic case of Lu/Hf = 0 in the urKREEP reservoir to constrain the minimum LMO differentiation age (the Lu/Hf in the urKREEP reservoir estimated by Warren (1989) is 0.13). However, model ages calculated assuming a Lu/Hf ratio closer to that measured for KREEP-rich samples, or determined from Hf isotopic growth trajectories for KREEP-rich samples (Sprung et al. 2013; Gaffney and Borg 2014), would yield a zircon urKREEP model age close to or older than the age of the solar system (Maurice et al. 2020). Furthermore, the zircon data demonstrate a systematic offset to lower epsilon Hf values compared to the bulk rock data that is not expected given the petrogenetic affinities between the KREEP-rich plutonic bulk rock samples and the zircons. Therefore, lunar solidification ages calculated using this approach are not consistent with an independent determination of the lunar differentiation time using W isotopes, or even the known age of the solar system.

Model ages for the formation of mare basalt sources determined using the ^{142}Nd–^{143}Nd systematics of mare basalts, and their isotopic linkage to other LMO solidification products, have been enabled by significant analytical advances over the past decade-and-a-half in highly precise measurements of $^{142}Nd/^{144}Nd$. Neodymium-142 is the decay product of the short-lived

and now extinct ^{146}Sm (^{146}Sm $t_{½}$ = 103 Ma), so measured variability in ^{142}Nd/^{144}Nd ratios reflects Sm/Nd fractionation that occurred earlier than about 4300 Ma. Neodymium-142 model ages represent the time that the mare basalt sources differentiated from a common bulk composition, requiring no specific assumption of the initial isotopic or elemental bulk composition of the Moon (see Borg et al. 2019, for the governing equations). Model ages calculated using the ^{146}Sm–^{142}Nd isotope system are: 4329 $^{+37}/_{-37}$ Ma (Nyquist et al. 1995), 4352 $^{+21}/_{-23}$ Ma (Rankenburg et al. 2006), 4313 $^{+25}/_{-30}$ Ma (Boyet and Carlson 2007), 4340 $^{+20}/_{-24}$ Ma (Brandon et al. 2009), 4341 $^{+14}/_{-15}$ Ma (McLeod et al. 2014), and 4331 $^{+35}/_{-37}$ Ma (Borg et al. 2019; Fig. 8). The uncertainties on all but the last stated age do not include uncertainty associated with the ^{146}Sm decay constant, which adds approximately 22 m.y. Notably, model ages determined by these six investigations are concordant. The measured ^{142}Nd/^{144}Nd–^{147}Sm/^{144}Nd values of FAS mineral separates are co-linear with these values determined for mare basalt sources (Borg et al. 2019; Fig. 8). The observation that these results define a single regression strongly supports the model assumption that the mare basalts are derived from magma sources that were in Nd isotopic equilibrium (i.e., had the same Nd isotopic composition) at the time that they formed, and furthermore, that the analyzed FAS mineral separates were also in Nd isotopic equilibrium with mare basalt sources at the time that the FAS samples crystallized. The time at which these materials were last in Nd isotopic equilibrium equilibration is calculated to be 4336 $^{+31}/_{-32}$ Ma (Borg et al. 2019). The co-linearity of these results is interpreted to indicate that the FAS samples and mare basalt sources formed from a common reservoir with a uniform Nd isotopic composition, within a short time interval. Furthermore, the initial ^{143}Nd/^{144}Nd compositions of several FAS and Mg-suite samples are essentially identical, and near-chondritic, indicating isotopic equilibrium among these sample suites at the time that they formed (Sio et al. 2020). Although Borg et al. (2019) evaluated several petrogenetic scenarios that could result in the observed Nd isotope systematics of the FAS and mare basalt samples, they conclude that these systematics most plausibly represent the formation of the mafic cumulate mare basalt sources and FAS flotation cumulates from a common source during LMO solidification at 4336 $^{+31}/_{-32}$ Ma.

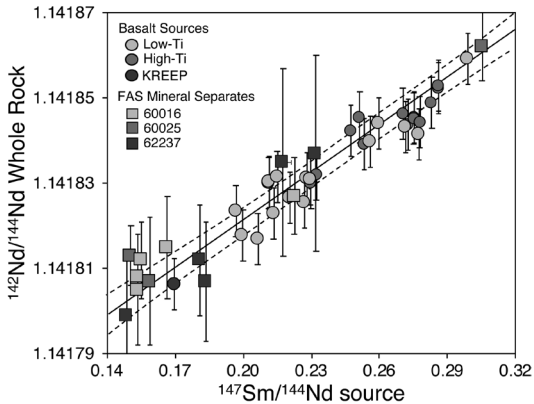

Figure 8. ^{142}Nd/^{144}Nd vs. ^{147}Sm/^{144}Nd isochron of lunar mantle and crust cumulates, as represented by mare basalt and KREEP basalt sources, and FAS sample mineral separates (Borg et al. 2011, 2019; Marks et al. 2019; Sio et al. 2020). The linear regression of all the data corresponds to an age of 4336 $^{+32}/_{-31}$ Ma. The dashed lines represent the uncertainty on the regression, and the uncertainty on the age includes an additional uncertainty component associated with the ^{146}Sm decay constant. [Reprinted from Earth and Planetary Science Letters, Vol. 523, Borg LE et al., Isotopic evidence for a young lunar magma ocean, Figure 7, Copyright (2019), with permission from Elsevier.]

Most of the model ages discussed here are concordant with the most reliable isochron ages for FAS and Mg-suite samples as well as the peak of Pb–Pb ages measured for zircons, and collectively, these results suggest that a major magmatic event occurred on the Moon around 4.34 to 4.37 Ga (Fig. 7). Ages determined from internal mineral isochrons measured for individual samples reflect the time at which the sample cooled below the closure temperature of the isotope system. Therefore, for samples that had extremely slow cooling histories (e.g., Elkins-Tanton et al. 2011; Borg et al. 2017), the isochron age of the sample can be significantly (up to about 60 m.y.) younger than the time at which the solid sample crystallized. Model ages that are defined by multiple samples, representing a broad geographic distribution on the Moon, are less likely to be affected by the cooling history of an individual sample, but rather represent a large-scale magmatic differentiation event. These include ^{182}Hf–^{182}W and ^{206}Pb–^{207}Pb model ages for lunar magma source formation, ^{146}Sm–^{142}Nd model ages for mare basalt source formation, and ^{147}Sm–^{143}Nd and ^{176}Lu–^{176}Hf model ages for urKREEP formation. These model ages represent the time at which these magma sources were last in isotopic and elemental equilibrium with each other, that is, the time at which these geochemical reservoirs formed from the bulk silicate Moon. If these reservoirs formed during primordial lunar differentiation, then the measured ages constrain the timing of LMO solidification to around 4.37 Ga. However, there are a few sample and model ages that are inconsistent with this interpretation: the Pb–Pb ages measured on a few zircon samples are up to about 40 Ma older than this differentiation age (Meyer et al. 1996; Grange et al. 2009, 2011; Nemchin et al. 2009a; Taylor et al. 2009); the Rb–Sr isochron age for dunite 74215 (Papanastassiou and Wasserburg 1975) as well as the Sm–Nd isochron ages for FAS samples 67016 and Y-86032 (Alibert et al. 1994; Nyquist et al. 2006) are similarly older than the proposed differentiation age of 4.37 Ga; and the older Hf model age determined from zircon analyses by Barboni et al. (2017) is inconsistent with primordial lunar differentiation at 4.37 Ga. If these older ages accurately record the timing of lunar magmatic events, then the preponderant age of ~4.37 Ga most likely represents a secondary magmatic event on the Moon, perhaps associated with mantle cumulate overturn. In this case, this event was geographically widespread, and produced isotopic equilibrium at this time among the sources of subsequent FAS, Mg-suite, KREEP and mare basalt magmatism, as represented by the near entirety of currently sampled silicate rocks and magma source regions on the Moon.

6. SYNTHESIS AND FUTURE DIRECTIONS

In the years since publication of New Views of the Moon I, our understanding of the processes that may have operated during solidification of a global magma ocean has advanced substantially. Key constraints are derived from detailed mapping of the compositional variability of the Moon's crust on a global scale, a well-defined chronology of the earliest lunar magmatic events, and fundamental crystallization experiments and physiochemical models designed to mimic processes operating during and in the immediate aftermath of magma ocean solidification. Although most of the recent work is designed and interpreted in the framework of solidification of a global magma ocean, some results reveal inconsistencies with the magma ocean model as it currently is defined. Integrating complex modeling, orbital remote sensing, and experimental studies into a petrological framework based on sample science and age determinations, as well as critically evaluating data and models, is crucial for our understanding of the formation and evolution of planetary bodies such as our Moon.

Orbital measurements that indicate that the Moon's average crustal thickness is 34 to 43 km and that the highland crust is compositionally heterogeneous provide strong constraints for experimental and physical models for crust formation. Lateral and vertical mineralogical heterogeneity within the lunar crust has been shown to exist, with farside feldspathic highlands

that are more magnesian than the nearside feldspathic highlands, and with lithologies ranging from anorthosites to norites, gabbroic anorthosites, gabbros, and anorthositic norites, as well as olivine-bearing outcrops, at a scale greater than the spatial resolution of the observations. In particular, the PAN lithology is posited to have a much higher purity than most samples returned by the Apollo missions, and future work is needed to constrain the extent of this unit and to evaluate its possible formation in the context of a magma ocean model or an alternative mode of formation. Future remote sensing investigations, specifically, coordinated observations across a wide spectral range, and lunar sample collections are also needed at the local scale (e.g., spatial resolutions on the order of meters) to better define the source regions of the olivine-bearing materials and constrain if and how the observed broad lithological heterogeneity was produced during LMO crystallization. Models and experiments based on remote observations of PAN and olivine-bearing lithologies are needed to establish whether these rocks are the product of an alternative lunar differentiation mode or secondary processes such as mantle overturn, a large impact, and/or post-magma ocean magmatism. Additionally, even though experimental investigations of LMO crystallization have produced KREEP-like compositions, the surface expression of KREEP is isolated to the nearside PKT. Future investigations should address this conundrum, and as a test of the magma ocean hypothesis, establish the geographic extent of KREEP. Ultimately, future work is needed to synthesize the key observations of the crustal dichotomy with the development of a unifying model of crustal formation.

Experimental investigations of magma ocean crystallization completed over the past decade have explored the effects of bulk composition, crystallization mode (equilibrium vs. fractional), pressure, and presence or absence of water on the petrology, geochemistry and stratigraphy that may ultimately result from magma ocean crystallization. The experimental results set the stage for new forward melting experiments and numerical models that explore the phase equilibria of post-overturn magma ocean cumulates, and their suitability as magma sources for Mg-suite samples, alkali-suite samples, mare basalts and picritic glasses. A goal for future experimental investigations is to explore potential processes in which LMO solidification and overturn occur contemporaneously. These results would enhance our understanding of both the compositional and thermal structure of the lunar interior.

Physiochemical modeling of the physical processes operating during and in the aftermath of magma ocean solidification provides a means to test predicted outcomes of magma ocean solidification against observations of the composition and distribution of lunar lithologic units, as well as parameters such as gravity, density, moment of inertia, and Love number. Key results from recent efforts to model magma ocean processes, in some cases using experimentally established physical constraints, indicate that the Moon was initially fully molten, that the Moon now possesses a small core, and that overturn and mixing among magma ocean crystallization products is an expected outcome from the gravitational instability that resulted from magma ocean crystallization. Degree-one overturn provides a mechanism to produce the observed compositional dichotomy in which Ti-rich and KREEP-rich materials are concentrated on the lunar nearside. The next generation of magma ocean physiochemical models will hopefully be built upon recent experimentally determined phase equilibria and rheological properties specific to the composition–temperature–pressure parameters of the Moon.

Many of the chronological constraints on ancient lunar magmatism indicate that a major magmatic event occurred on the Moon around 4.34 to 4.37 Ga. This age is reflected in the most reliable isochron ages for FAS and Mg-suite samples, in the peak of Pb–Pb ages measured for zircons, and also in model ages determined using short-lived as well as long-lived isotope systems. These model ages represent the time at which these magma sources were last in isotopic and elemental equilibrium. If these ages represent primordial solidification of the LMO, then this constrains the timing of initial lunar differentiation to around 4.37 Ga. This interpretation, however, is not consistent with the Pb–Pb ages measured on a few zircon samples that are up to

about 40 Ma older than this age. If these ancient ages represent primordial lunar differentiation at about 4.5 Ga, then a secondary magmatic event must have occurred on the Moon that was widespread and produced isotopic equilibrium at 4.37 Ga among the sources of subsequent FAS, Mg-suite, KREEP and mare basalt magmatism. Resolving the origin of the magmatic event at 4.37 Ga remains a significant outstanding challenge for the magma ocean hypothesis.

The integrated results of the past decade-and-a-half of study of lunar differentiation continue to demonstrate the complex geologic history of our Moon and underscore the need for continued study of lunar samples, experimental work, and the acquisition of new lunar samples from locations carefully selected to address outstanding questions. With this new body of work, the longstanding magma ocean model continues to be tested, and old and new models, ranging from a heterogeneous magma ocean, to serial magmatism, an impact modified crust, heat pipe magmatism, and cumulate mantle overturn during or after solidification of the LMO, continue to be explored. Future sample return from targeted geological field locations, in-situ geophysical measurements, and high-spatial-resolution remote sensing mapping coupled with computational models, laboratory experiments, and geochronological dating will provide new tests for lunar differentiation models. Abundant research avenues remain for current and future generations to investigate the early geological evolution of our nearest planetary neighbor, and the next phase of lunar exploration and science will help us to better understand the Earth-Moon system and the early evolution of rocky planets in general through space and time.

ACKNOWLEDGMENTS

We are grateful for Paul Warren's contributions to the early development of this chapter. AMG thanks Kelsey Woody for her efforts in compiling the bibliography for this chapter. This work was supported by NASA grant 80NSSC18K0249 to ND, and NASA grant 80NSSC19K0558 to JG. WvW thanks the Dutch Research Council (NWO) and the Netherlands Space Office (NSO) User Support Program for financial support. KBP received financial support for this contribution from the McDonnell Center for Space Sciences at Washington University in St. Louis and a NASA Earth and Space Sciences Fellowship. This work was performed under the auspices of the U.S. Department of Energy by Lawrence Livermore National Laboratory under Contract DE-AC52-07NA27344; LLNL-BOOK-813350.

REFERENCES

Alibert C, Norman MD, McCulloch MT (1994) An ancient Sm–Nd age for a ferroan noritic anorthosite clast from lunar breccia 67016. Geochim Cosmochim Acta 58:2921–2926

Antonangeli D, Morard G, Schmerr NC, Komabayashi T, Krisch M, Fiquet G, Fei Y (2015) Towards a mineral physics reference model for the Moon's core. Proc Nat Acad Sci 112:3916–3919

Arai T, Takeda H, Yamaguchi A, Ohtake M (2008) A new model of lunar crust: asymmetry in crustal composition and evolution. Earth Planets Space 60:433–444

Arnold JA, Glotch TD, Lucey PG, Song E, Thomas IR, Bowles NE, Greenhagen BT (2016) Constraints on olivine-rich rock types on the Moon as observed by Diviner and M3: Implications for the formation of the lunar crust. J Geophys Res: Planets 121:1342–1361

Baker DMH, Head JW (2015) Constraints on the depths of origin of peak rings on the Moon from the Moon Mineralogy Mapper data. Icarus 258:164–180

Barboni M, Boehnke P, Keller B, Kohl IE, Schoene B, Young ED, McKeegan KD (2017) Early formation of the Moon 4.51 billion years ago. Sci Adv 3:e1602365

Bombardieri DJ, Norman MD, Kamenetsky VS, Danyushevsky LV (2005) Major element and primary sulfur concentrations in Apollo 12 mare basalts: The view from melt inclusions. Meteorit Planet Sci 40:679–693

Borg L, Norman MD, Nyquist L, Bogard D, Snyder G, Taylor L, Lindstrom M (1999) Isotopic studies of ferroan anorthosite 62236; a young lunar crustal rock from a light rare-earth-element-depleted source. Geochim Cosmochim Acta 63:2679–2691

Borg LE, Connelly JN, Boyet M, Carlson RW (2011) Chronological evidence that the Moon is either young or did not have a global magma ocean. Nature 477:70–72

Borg LE, Gaffney AM, Shearer CK (2015) A review of lunar chronology revealing a preponderance of 4.34–4.37 Ga ages. Meteorit Planet Sci 50:715–732
Borg LE, Connelly JN, Cassata W, Gaffney AM, Bizzarro M (2017) Chronologic implications for slow cooling of troctolite 76535 and temporal relationships between the Mg-suite and the ferroan anorthosite suite. Geochim Cosmochim Acta 201:377–291
Borg LE, Gaffney AM, Kruijer TS, Marks NA, Sio CK, Wimpenny J (2019) Isotopic evidence for a young lunar magma ocean. Earth Planet Sci Lett 523:115706
Boujibar A, Andrault D, Bouhifd MA, Bolfan–Casanova N, Devidal J–L, Trcera N (2014) Metal–silicate partitioning of sulphur, new experimental and thermodynamic constraints on planetary accretion. Earth Planet Sci Lett 391:42–54
Boukaré CE, Parmentier EM, Parman SW (2018) Timing of mantle overturn during magma ocean solidification. Earth Planet Sci Lett 491:216–225
Boyet M, Carlson RW (2007) A highly depleted moon or a non-magma ocean origin for the lunar crust? Earth Planet Sci Lett 262:505–516
Brandon AD, Lapen TJ, Debaille V, Beard BL, Rankenburg K, Neal C (2009) Re-evaluating $^{142}Nd/^{144}Nd$ in lunar mare basalts with implications for the early evolution and bulk Sm/Nd of the Moon. Geochim Cosmochim Acta 73:6421–6445
Brown SM, Grove TL (2015) Origin of the Apollo 14, 15, and 17 yellow ultramafic glasses by mixing of deep cumulate remelts. Geochim Cosmochim Acta 171:201–215
Buck W, Toksöz M (1980) The bulk composition of the moon based on geophysical constraints. Proc Lunar Planet Sci Conf 11:2043–2058
Cahill JTS, Lucey PG, Wieczorek MA (2009) Compositional variations of the lunar crust: Results from radiative transfer modelling of central peak spectra. J Geophys Res 114:E09001
Canup RM (2012) Forming a Moon with an Earth-like composition via a giant impact. Science 338:1052–1055
Canup RM, Righter K, Dauphas N, Pahlevan K, Ćuk M, Lock SJ, Stewart ST, Salmon J, Rufu R, Nakajima M, Magna T (2023) Origin of the Moon. Rev Mineral Geochem 89:53–102
Carlson RW, Lugmair GW (1979) Sm–Nd constraints on early lunar differentiation and the evolution of KREEP. Earth Planet Sci Lett 45:123–132
Carlson RW, Lugmair GW (1981a) Sm–Nd age of lherzolite 67667—Implications for the processes involved in lunar crustal formation. Earth Planet Sci Lett 56:1–8
Carlson RW, Lugmair GW (1981b) Time and duration of lunar highlands crust formation. Earth Planet Sci Lett 52:227–238
Carlson RW, Lugmair GW (1988) The age of ferroan anorthosite 60025—Oldest crust on a young moon? Earth Planet Sci Lett 90:119–130
Carlson RW, Borg LE, Gaffney AM, Boyet M (2014) Rb–Sr, Sm–Nd and Lu–Hf isotope systematics of the lunar Mg-suite: the age of the lunar crust and its relation to the time of Moon formation. Phil Trans R Soc A 372:20130246
Charlier B, Grove TL, Namur O, Holtz F (2018) Crystallization of the lunar magma ocean and the primordial mantle–crust differentiation of the Moon. Geochim Cosmochim Acta 234:50–69
Cheek LC, Donaldson Hanna KL Pieters CM, Head JW, Whitten JL (2013) The distribution and purity of anorthosite across the Orientale basin: New perspectives from Moon Mineralogy Mapper data. J Geophys Res 118:1805–1820
Chen EMA, Nimmo F (2016) Tidal dissipation in the lunar magma ocean and its effect on the early evolution of the Earth–Moon system. Icarus 275:132–142
Chen Y, Zhang Y, Liu Y, Guan Y, Eiler J, Stolper EM (2015) Water, fluorine, and sulfur concentrations in the lunar mantle. Earth Planet Sci Lett 427:37–46
Chi H, Dasgupta R, Duncan MS, Shimizu N (2014) Partitioning of carbon between Fe–rich alloy melt and silicate melt in a magma ocean – implications for the abundance and origin of volatiles in Earth, Mars, and the Moon. Geochim Cosmochim Acta 139:447–471
Compston W, Foster JJ, Gray CM (1975) Rb–Sr ages of clasts within Boulder 1, Station 2, Apollo 17. The Moon 14:445–462
Connelly JN, Bizzarro M (2016) Lead isotope evidence for a young formation age of the Earth–Moon system. Earth Planet Sci Lett 452:36–43
Corley LM, McGovern PJ, Kramer GY, Lemelin M, Trang D, Gillis-Davis JJ, Taylor GJ, Powell KE, Kiefer WS, Wieczorek M, Zuber MT (2018) Olivine-bearing lithologies on the Moon: Constraints on origins and transport mechanisms from M3 spectroscopy, radiative transfer modelling, and GRAIL crustal thickness. Icarus 300:287–304
Crites ST, Lucey PG (2015) Revised mineral and Mg# maps of the Moon from integrating results from the Lunar Prospector neutron and gamma-ray spectrometers with Clementine spectroscopy. Am Mineral 100:973–982
Crow CA, McKeegan KD, Moser DE (2017) Coordinated U–Pb geochronology, trace element, Ti-in-zircon thermometry and microstructural analysis of Apollo zircons. Geochim Cosmochim Acta 202:264–284
Davenport JD (2013) The Igneous SPICEs Suite: old programs with a new look. Planet Sci Res Disc Rep 1:173
Day JMD (2019) Geochemical constraints on residual metal and sulfide in the sources of lunar mare basalts. Am Mineral 11:1734–1740
De Vries J, van den Berg A, van Westrenen W (2010) The formation and evolution of a lunar core from ilmenite-rich magma ocean cumulates. Earth Planet Sci Lett 292:139–147

Dimanov A, Dresen G (2005) Rheology of synthetic anorthite–diopside aggregates: Implications for ductile shear zones. J Geophys Res 110:B07203

Ding S, Hough T, Dasgupta R (2018) New high pressure experiments on sulfide saturation of high-FeO* basalts with variable TiO_2 contents—Implications for the sulfur inventory of the lunar interior. Geochim Cosmochim Acta 222:319–339

Donaldson Hanna KL, Cheek LC, Pieters CM, Mustard JF, Greenhagen BT, Thomas IR, Bowles NE (2014) Global assessment of pure crystalline plagioclase across the Moon and implications for the evolution of the primary crust. J Geophys Res: Planets 119:1516–1545

Dygert N, Hirth G, Liang Y (2016) A flow law for ilmenite in dislocation creep: Implications for lunar cumulate mantle overturn. Geophys Res Lett 43:532–540

Dygert N, Liang Y, Hess P (2013) The importance of melt TiO_2 in affecting major and trace element partitioning between Fe–Ti oxides and lunar picritic glass melts. Geochim Cosmochim Acta 106:134–151

Dygert N, Liang Y, Sun C, Hess P (2014) An experimental study of trace element partitioning between augite and Fe-rich basalts. Geochim Cosmochim Acta 132:170–186

Dygert N, Lin J-F, Marshall EW, Kono Y, Gardner JE (2017) A low viscosity lunar magma ocean forms a stratified anorthitic flotation crust with mafic poor and rich units. Geophys Res Lett 44:10.1002/2017GL075703

Dygert NJ, Draper DS, Rapp JF, Lapen TJ, Fagan AL, Neal CR (2020) Experimental determinations of trace element partitioning between plagioclase, pigeonite, olivine, and lunar basaltic melts and an fO_2 dependent model for plagioclase-melt Eu partitioning. Geochim Cosmochim Acta 279:258–280

Edmunson J, Nyquist LE, Borg LE (2007) Sm–Nd Isotopic Systematics of Troctolite 76335, Lunar Planet Sci Conf Abstracts 38:#1962

Edmunson J, Borg LE, Nyquist LE, Asmerom Y (2009) A combined Sm–Nd, Rb–Sr, and U–Pb isotopic study of Mg-suite norite 78238: Further evidence for early differentiation of the Moon. Geochim Cosmochim Acta 73:514–527

Elardo SM, Draper DS, Shearer CK (2011) Lunar Magma Ocean crystallization revisited: Bulk composition, early cumulate mineralogy, and the source regions of the highlands Mg-suite. Geochim Cosmochim Acta 75:3024–3045

Elardo SM, McCubbin FM, Shearer Jr CK (2012) Chromite symplectites in Mg-suite troctolite 76535 as evidence for infiltration metasomatism of a lunar layered intrusion. Geochim Cosmochim Acta 87:154–177

Elardo SM, Shearer CK, Vander Kaaden KE, McCubbin FM, Bell AS (2015) Petrogenesis of primitive and evolved basalts in a cooling Moon: Experimental constraints from the youngest known lunar magmas. Earth Planet Sci Lett 422:126–137

Elardo SM, Laneuville M, McCubbin FM Shearer CK (2020) Early crust building enhanced on the Moon's nearside by mantle melting-point depression. Nat Geosci 13:339–343

Elardo SM, Pieters CM, Dhingra D, Donaldson Hanna KL, Glotch TD, Greenhagen BT, Gross J, Head JW, Jolliff BL, Klima RL, Magna T, McCubbin FM, Ohtake M (2023) The evolution of the lunar crust. Rev Mineral Geochem 89:293–338

Elkins-Tanton LT (2008) Linked magma ocean solidification and atmospheric growth for Earth and Mars. Earth Planet Sci Lett 271:181–191

Elkins-Tanton LT (2012) Magma oceans in the inner solar system. Annu Rev Earth Planet Sci 40:113–139

Elkins-Tanton LT, Hager BH, Grove TL (2004) Magmatic effects of the lunar late heavy bombardment. Earth Planet Sci Lett 222:17–27

Elkins-Tanton L T, Burgess S, Yin Q-Z (2011) The lunar magma ocean: Reconciling the solidification with lunar petrology and geochronology. Earth Planet Sci Lett 304:326–336

Elphic RC, Lawrence DJ, Feldman WC, Barraclough BL, Maurice S, Binder AB, Lucey PG (2000) Lunar rare earth element distribution and ramifications for FeO and TiO_2: Lunar Prospector neutron spectrometer observations. J Geophys Res 105: 20333–20345

Fischer-Gödde M, Becker H, Wombacher F (2011) Rhodium, gold and other highly siderophile elements in orogenic peridotites and peridotite xenoliths. Chem Geol 280:365–383

Friedman AM, Milsted J, Metta D, Henderson D, Lerner J, Harkness AL, Rokop DJ (1966) Alpha decay half lives of ^{148}Gd, ^{150}Gd and ^{146}Sm. Radiochim Acta 5:192–194

Gaddis LR, Joy KH, Bussey BJ, Carpenter JD, Crawford IA, Elphic RC, Halekas JS, Lawrence SJ, Xiao L (2023) Recent exploration of the Moon: Science from lunar missions since 2006. Rev Mineral Geochem 89:1–51

Gaffney AM, Borg LE (2014) A young solidification age for the lunar magma ocean. Geochim Cosmochim Acta 140:227–240

Gaffney AM, Borg LE, Asmerom Y, Shearer CK, Burger PV (2011) Disturbance of isotope systematics during experimental shock and thermal metamorphism of a lunar basalt with implications for Martian meteorite chronology. Meteorit Planet Sci 46:35–52

Gaffney AM, Borg LE, Shearer CK, Burger PV (2015) Chronology of 15445 norite clast B and implications for Mg-suite magmatism. Lunar Planet Sci Conf 46:1443

Garcia RF, Gagnepain-Beyneix J, Chevrot S, Lognonné P (2011) Very preliminary reference Moon model. Phys Earth Planet Int 202–203:89–91

Garcia RF, Gagnepain-Beyneix J, Chevrot S, Lognonné P (2012) Erratum to "Very preliminary reference Moon model". Phys Earth Planet Int 202–203:89–91
Giguere TA, Taylor GJ, Hawke BR, Lucey PG (2000) The titanium contents of lunar mare basalts. Meteorit Planet Sci 35:193–200
Gillis JJ, Jolliff BJ, Korotev RL (2004) Lunar surface geochemistry: Global concentrations of Th, K, and FeO as derived from lunar prospector and Clementine data. Geochim Cosmochim Acta 68:3791–3805
Grange ML, Nemchin AA, Pidgeon RT, Timms N, Muhling JR, Kennedy AK (2009) Thermal history recorded by the Apollo 17 impact melt breccia 73217. Geochim Cosmochim Acta 73:3093–3107
Grange ML, Nemchin AA, Timms N, Pidgeon RT, Meyer C (2011) Complex magmatic and impact history prior to 4.1 Ga recorded in zircon from Apollo 17 South Massif aphanitic breccia 73235. Geochim Cosmochim Acta 75:2213–2232
Grange ML, Nemchin AA, Pidgeon RT (2013a) The effect of 1.9 and 1.4 Ga impact events on 4.3 Ga zircon and phosphate from an Apollo 15 melt breccia. J Geophys Res: Planets 118:2180–2197
Grange ML, Pidgeon RT, Nemchin AA, Timms NE, Meyer C (2013b) Interpreting U–Pb data from primary and secondary features in lunar zircon. Geochim Cosmochim Acta 101:112–132
Greenhagen BT, Lucey PG, Wyatt MB, Glotch TD, Allen CC, Arnold JA, Bandfield JL, Bowles NE, Hanna KL, Hayne PO, Song E (2010) Global silicate mineralogy of the Moon from the Diviner Lunar Radiometer. Science 329:1507–1509
Gross J, Joy KH (2016) Evolution, lunar: From magma ocean to crust formation. *In*: Cudnik B (ed) Encyclopedia of Lunar Science. Springer, Cham.
Gross J, Treiman AH, Mercer CN (2014) Lunar feldspathic meteorites: Constraints on the geology of the lunar highlands, and the origin of the lunar crust. Earth Planet Sci Lett 388:318–328
Gross J, Hilton A, Prissel TC, Setera JB, Korotev RL, Calzada-Diaz A (2020) Geochemistry and petrogenesis of northwest Africa 10401: A new type of the Mg-suite rocks. J Geophys Res:Planets 125:1–24
Hammer JE, Shea T, Taylor GJ, Hellebrand E, Welsch B (2017) Magmatic cooling history of troctolite 76535 constrained by diffusion modeling of olivine and plagioclase compositional zonation. Lunar Planet Sci Conf 48:1274
Harada Y, Goossens S, Matsumoto K, Yan J, Ping J, Noda H, Haruyama J (2014) Strong tidal heating in an ultralow-viscosity zone at the core–mantle boundary of the Moon. Nat Geosci 7:569–572
Harada Y, Goossens S, Matsumoto K, Yan J, Ping J, Noda H, Haruyama J (2016) The deep lunar interior with a low-viscosity zone: Revised constraints from recent geodectic parameters on the tidal response of the moon. Icarus 276:96–101
Haskin LA, Lindstrom MM, Salpas PA, Lindstrom DJ (1981) On compositional variations among lunar anorthosites. Proc Lunar Planet Sci Conf 12:41–66
Haskin LA, Korotev RL, Rockow KM, Jolliff BL (1998) The case for an Imbrium origin of the Apollo thorium-rich impact-melt breccias. Meteorit Planet Sci 33:959–975
Haskin LA, Gillis JJ, Korotev RL, Jolliff BL (2000) The materials of the lunar Procellarum KREEP Terrane: A synthesis of data from geomorphological mapping, remote sensing, and sample analyses. J Geophys Res Planets 105:20403–20415
Haskin LA, Moss BE, McKinnon WB (2003) On estimating contributions of basin ejecta to regolith deposits at lunar sites. Meteorit Planet Sci 38:3–33
Hauck SA, Aurnou JM, Dombard AJ (2006) Sulfur's impact on core evolution and magnetic field generation on Ganymede. J Geophys Res:Planets 111:E09008
Hauri EH, Saal AE, Rutherford MJ, van Orman JA (2015) Water in the Moon's interior: Truth and consequences. Earth Planet Sci Lett 409:252–264
Hawke BR, Peterson CA, Blewett DT, Bussey DBJ, Lucey PG, Taylor GJ, Spudis PD (2003) Distribution and modes of occurrence of lunar anorthosite. J Geophys Res 108:5050
Hess PC, Parmentier EM (1995) A model for the thermal and chemical evolution fo the Moon's interior: implications for the onset of mare volcanism. Earth Planet Sci Lett 134:501–514
Hess PC, Parmentier EM (2001) Thermal evolution of a thicker KREEP liquid layer. J Geophys Res 106:28023–28032
Hirth G, Kohlstedt DL (2004) Rheology of the upper mantle and the mantle wedge: A view from the experimentalists. *In:* Eiler J (ed) Inside the Subduction Factory, Geophysical Monograph Series. Am Geophys Union, p 83–105
Hood LL, Zakharian A, Halekas J, Mitchell DL, Lin RP, Acuna MH, Binder AB (2001) Initial mapping and interpretation of lunar crustal magnetic anomalies using Lunar Prospector magnetometer data. J Geophys Res 106:27825–27839
Hopkins MD, Mojzsis SJ (2015) A protracted timeline for lunar bombardment from mineral chemistry, Ti thermometry and U–Pb geochronology of Apollo 14 melt breccia zircons. Contrib Mineral Petrol 169:30
Huet B, Yamato P, Grasemann B (2014) The minimized power geometric model: an analytical mixing model for calculating polyphase rock viscosities consistent with experimental data. J Geophys Res: Solid Earth 119:3897–3924
Hurwitz DM, Kring DA (2014) Differentiation of the South Pole–Aitken basin impact melt sheet: Implications for lunar exploration. J Geophys Res 119:1110–1133
Jing Z, Wang Y, Kono Y, Yu T, Sakamaki T, Park C, Rivers ML, Sutton SR, Shen G (2014) Sound velocity of Fe–S liquids at high pressure: Implications for the Moon's molten outer core. Earth Planet Sci Lett 396:78–87

Jolliff BL, Haskin LA (1995) Cogenetic rock fragments from a lunar soil: Evidence of a ferroan noritic-anorthosite pluton on the Moon. Geochim Cosmochim Acta 59:2345–2374
Jolliff BL, Gillis JJ, Haskin LA, Korotev RL, Wieczorek MA (2000) Major lunar crustal terranes: Surface expressions and crust-mantle origins. J Geophys Res 105:4197–4216
Jordan PG (1987) The deformational behavior of bimineralic limestone-halite aggregates. Tectonophys 135:185–197
Joy KH, Gross J, Korotev RL, Zeigler RA, McCubbin FM, Snape JF, Curran NM, Pernet-Fisher JF, Arai T (2023) Lunar Meteorites. Rev Mineral Geochem 89:509–562
Khan A, Connolly JAD, Pommier A, Noir J (2014) Geophysical evidence for melt in the deep lunar interior and implications for lunar evolution. J Geophys Res Planets 119:2197–2221
Khan A, Connolly JA, Maclennan J, Mosegaard K (2007) Joint inversion of seismic and gravity data for lunar composition and thermal state. Geophys J Int 168:243–258
Kleine T, Palme H, Mazger K, Halliday AN (2005) Hf–W chronometry of lunar metals and the age and early differentiation of the Moon. Science 310:1671–1674
Klima RL, Pieters CM, Boardman JW, Green RO, Head III J W, Isaacson PJ, Mustard JF, Nettles JW, Petro NE, Staid MI, Sunshine JM, Taylor LA, Tompkins S (2011) New insights into lunar petrology: Distribution and composition of prominent low-Ca pyroxene exposures as observed by the Moon Mineralogy Mapper (M^3). J Geophys Res 116:E00G06
Kollé JJ, Blacic JD (1983) Deformation of single-crystal clinopyroxenes: 1. Mechanical twinning in diopside and hedenbergite. J Geophys Res 87:4019–4034
Korotev RL (2005) Lunar geochemistry as told by lunar meteorites. Chemie der Erde 65:297–346
Korotev RL, Jolliff BL, Zeigler RA, Gillis JJ, Haskin LA (2003) Feldspathic lunar meteorites and their implications for compositional remote sensing of the lunar surface and the composition of the lunar crust. Geochim Cosmochim Acta 67:4895–4923
Korotev RL, Jolliff BL, Zeigler RA (2010) On the origin of the Moon's feldspathic highlands, pure anorthosite, and the feldspathic lunar meteorites. Lunar Planet Sci Conf 41:1533
Kramer GY, Kring DA, Nahm AL, Pieters CM (2013) Spectral and photogeologic mapping of Schrodinger Basin and implications for post-South Pole-Aitken impact deep subsurface stratigraphy. Icarus 223:131–148
Krawczynski MJ, Grove TL (2012) Experimental investigation of the influence of oxygen fugacity on the source depths for high titanium lunar ultramafic magmas. Geochim Cosmochim Acta 79:1–19
Kruijer TS, Kleine T (2017) Tungsten isotopes and the origin of the Moon. Earth Planet Sci Lett 475:15–24
Kruijer TS, Kleine T, Fischer-Gödde M, Sprung P (2015) Lunar tungsten isotopic evidence for the late veneer. Nature 520:534–537
Laneuville M, Wieczorek MA, Breuer D, Aubert J, Morard G, Rückriemen T (2014) A long–lived lunar dynamo powered by core crystallization. Earth Planet Sci Lett 401:251–260
Lawrence DJ, Elphic RC, Feldman WC, Prettyman TH (2003) Small-area thorium features on the lunar surface. J Geophys Res 108:5102
Lemelin M, Lucey PG, Song E, Taylor GJ (2015) Lunar central peak mineralogy and iron content using the Kaguya Multiband Imager: Reassessment of the compositional structure of the lunar crust. J Geophys Res Planets 120:869–887
Li H, Zhang N, Liang Y, Wu B, Dygert NJ, Huang J, Parmentier EM (2019) Lunar cumulate mantle overturn: A model constrained by ilmenite rheology. J Geophys Res Planets 124:1357–1378
Lin Y, Tronche EJ, Steenstra ES, van Westrenen W (2017a) Evidence for an early wet Moon from experimental crystallization of the lunar magma ocean. Nat Geosci 10:14–18
Lin Y, Tronche EJ, Steenstra ES, van Westrenen W (2017b) Experimental constraints on the solidification of a nominally dry lunar magma ocean. Earth Planet Sci Lett 471:104–116
Lin Y, Hui H, Xia X, Shang S, van Westrenen W (2019) Experimental constraints on the solidification of a hydrous lunar magma ocean. Meteorit Planet Sci 55:207–230
Lock SJ, Stewart ST, Petaev MI, Leinhardt ZM, Mace M, Jacobsen SB, Ćuk M (2016) The origin of the Moon within a terrestrial synestia. J Geophys Res: Planets 123:910–951
Lodders K (2003) Solar System abundances and condensation temperatures of the elements. Astrophys J 591:1220–1247
Longhi J (1991) Comparative liquidus equilibria of hypersthene-normative basalts at low pressure. Am Mineral 76:785–800
Longhi J (2003) A new view of lunar ferroan anorhotistes: postmagma ocean petrogenesis. J Geophys Res 108:5083
Longhi J (2006) Petrogenesis of picritic mare magmas: constraints on the extent of early lunar differentiation. Geochim Cosmochim Acta 70:5919–5934
Lucey PG (2004) Mineral maps of the Moon. Geophys Res Lett 31:L08701
Lucey PG, Blewett DT, Hawke BR (1998) Mapping the FeO and TiO_2 content of the lunar surface with multispectral imagery. J Geophys Res 103:3679–3699
Lucey PG, Norman JA, Crites ST, Taylor GJ, Hawke BR, Lemelin M, Melosh HJ (2014) A large spectral survey of small lunar craters: Implications for the composition of the lunar mantle. Am Mineral 99:2251–2257
Lugmair GW, Marti K, Kurtz JP, Scheinin NB (1976) History and genesis of lunar troctolite 76535 or: How old is old? Proc Lunar Planet Sci Conf 7:2009–2033

Marks N, Borg L, Gaffney A, Shearer C, Burger P (2014) Additional evidence for young ferroan anorthositic magmatism on the Moon from Sm–Nd isotopic measurements of 60016 clast 3A. Lunar Planet Sci Conf 45:1129
Marks NE, Borg LE, Shearer CK, Cassata WS (2019) Geochronology of an Apollo 16 clast provides evidence for a basin-forming impact 4.3 billion years ago. J Geophys Res: Planets 124:2465–2481
Martinot M, Besse S, Flahaut J, Quantin-Nataf C, Lozac'h L, van Westrenen W (2018) Mineralogical diversity and geology of humboldt crater derived using Moon Mineralogy Mapper data. J Geophys Res: Planets 123:612–629
Martinot M, Flahaut J, Besse S, Quantin-Nataf C, van Westrenen W (2020) Mineralogical survey of the anorthositic Feldspathic Highlands Terrane crust using Moon Mineralogy Mapper data. Icarus 113747
Matsuyama I, Nimmo F, Keane JT, Chan NH, Taylor GJ, Wieczorek MA, Kiefer WS, Williams JG (2016) GRAIL, LLR, and LOLA constraints on the interior structure of the Moon. Geophys Res Lett 42:8365–8375
Maurice M, Tosi N, Schwinger S, Breuer D, Kleine T (2020) A long-lived magma ocean on a young Moon. Sci Adv 6:eaba8949
Maurice M, Tosi N, Samuel H, Plesa A-C, Hüttig C, Breuer D (2017) Onset of solid-state mantle convection and mixing during magma ocean solidification. J Geophys Res: Planets 122:577–598
McCallum IS, O'Brien HE (1996) Stratigraphy of the lunar highland crust: Depths of burial of lunar samples from cooling-rate studies. Am Mineral 81:1166–1175
McCallum IS, Schwartz JM (2001) Lunar Mg suite: Thermobarometry and petrogenesis of parental magmas. J Geophys Res: Planets 106:27969–27983
McCallum IS, Domeneghetti MC, Schwartz JM, Mullen EK, Zema M, Cámara F, McCammon C. Ganguly J (2006) Cooling history of lunar Mg-suite gabbronorite 76255, troctolite 76535 and Stillwater pyroxenite SC-936: The record in exsolution and ordering in pyroxenes. Geochim Cosmochim Acta 70:6068–6078
McCubbin FM, Barnes JJ, Ni P, Hui H, Klima RL, Burney D, Day JMD, Magna T, Boyce JW, Tartèse R, Vander Kaaden KE, Steenstra E, Elardo SM, Zeigler RA, Anand M, Liu Y (2023) Endogenous lunar volatiles. Rev Mineral Geochem 89:729–786
McDonough WF, Sun S-S (1995) The composition of the Earth. Chem Geol 120:223–253
McLeod CL, Brandon AD, Armytage RMG (2014) Constraints on the formation age and evolution of the Moon from ^{142}Nd–^{143}Nd systematics of Apollo 12 basalts. Earth Planet Sci Lett 396:179–189
Meyer C, Williams IS, Compston W (1996) Uranium-lead ages for lunar zircons: Evidence for a prolonged period of granophyre formation from 4.32 to 3.88 Ga. Meteorit Planet Sci 31:370–387
Meyer J, Elkins-Tanton L, Wisdom J (2010) Coupled thermal-orbital evolution of the early Moon. Icarus 208:1–10
Meissner F, Schmidtott WD, Ziegler L (1987) Half-life and alpha-ray energy of Sm-146. Z Phys A 327:171–174
Moore WB, Simon JI, Webb AAG (2017) Heat-pipe planets. Earth Planet Sci Lett 474:13–19
Moriarty DP, Pieters CM, Isaacson PJ (2013) Compositional heterogeneity of central peaks within the South Pole-Aitken basin. J Geophys Res Planets 118:2310–2322
Morrison DA (1998) Did a thick South Pole-Aitken Basin melt sheet differentiate to form cumulates? Lunar Planet Sci Conf 44:3039
Mougel B, Moynier F, Göpel C (2018) Chromium isotopic homogeneity between the Moon, the Earth, and enstatite chondrites. Earth Planet Sci Lett 481:1–8
Nakamura N, Tatsumoto M, Nunes PD, Unruh DM, Schwab AB, Wildeman TR (1976) 4.4 b.y.-old clast in Boulder 7, Apollo 17: a comprehensive chronological study by U–Pb, Rb–Sr and Sm–Nd methods. Proc 7th Lunar Sci Conf 2309–2333
Nakamura R, Matsunaga T, Ogawa Y, Yamamoto S, Hiroi T, Saiki K, Hirata N, Arai T, Kitazato K, Takeda H, Sugihara T, Kodama S, Ohtake M, Haruyama J, Yokota Y (2009) Ultramafic impact melt sheet beneath the South Pole-Aitken basin on the Moon. Geophys Res Lett 36:22202
Nekvasil H, Lindsley DH, DiFrancesco N, Catalano T, Coraor AE, Charlier B (2015) Uncommon behavior of plagioclase and the ancient lunar crust. Geophys Res Lett 42:10–573
Nemchin AA, Whitehouse MJ, Pidgeon RT, Meyer C (2006) Oxygen isotopic signature of 4.4–3.9 Ga zircons as a monitor of differentiation processes on the Moon. Geochim Cosmochim Acta 70:1864–1872
Nemchin AA, Pidgeon RT, Whitehouse MJ, Vaughan J P, Meyer C (2008) SIMS U–Pb study of zircon from Apollo 14 and 17 breccias: Implications for the evolution of lunar KREEP. Geochim Cosmochim. Acta 72:668–689
Nemchin A, Timms N, Pidgeon R, Geisler T, Reddy S, Meyer C (2009a) Timing of crystallization of the lunar magma ocean constrained by the oldest zircon. Nat Geosci 2:133–136
Nemchin AA, Pidgeon RY, Healy D, Grange ML, Whitehouse MJ, Vaughan JP (2009b) The comparative behaviour of apatite-zircon U–Pb systems in Apollo 14 breccias: Implications for the history of the Fra Mauro formation. Meteorit Planet Sci 44:1717–1734
Nemchin AA, Jeon H, Bellucci JJ, Timms NE, Snape JF, Kilburn MR, Whitehouse MJ (2017) Pb–Pb ages of feldspathic clasts in two Apollo 14 breccia samples. Geochim Cosmochim Acta 217:441–461
Norman MD, Borg LE, Nyquis LE, Bogard DE (2003) Chronology, geochemistry, and petrology of a ferroan noritic anorthosite clast from Descartes breccia 67215; clues to the age, origin, structure, and impact history of the lunar crust. Meteorit Planet Sci 38:645–661
Nyquist LE, Shih C-Y (1992) The isotopic record of lunar volcanism. Geochim Cosmochim Acta 56:2213–2234

Nyquist LE, Reimold WU, Bogard DD, Wooden JL, Bansal BM, Weismann H, Shih C-Y (1981) A comprehensive Rb–Sr, Sm–Nd, and K–Ar study of shocked norite 78236: Evidence of slow cooling in the lunar crust? Proc Lunar Planet Sci Conf 12:B67–B97

Nyquist LE, Wiesmann H, Bansal B, Shih C-Y, Keith JE, Harper CL (1995) ^{146}Sm–^{142}Nd formation interval for the lunar mantle. Geochim Cosmochim Acta 59:2817–2837

Nyquist L, Bogard D, Yamaguchi A, Shih C-Y, Karouji Y, Ebihara M, Reese Y, Garrison D, McKay G,Takeda H (2006) Feldspathic clasts in Yamato-86032: Remnants of the lunar crust with implications for its formation and impact history. Geochim Cosmochim Acta 70:5990

Nyquist LE, Shih CY, Reese YD (2012) Redetermination of the Sm–Nd age and initial ε_{Nd} of lunar troctolite 76535: Implications for lunar crustal development. Lunar Planet Sci Conf 43:2416

Ogawa Y, Matsunaga T, Nakamura R, Saiki K, Ohtake M, Hiroi T, Takeda H, Arai T, Yokota Y, Yamamoto S, Hirata N, Sugihara T, Sasaki S, Haruyama J, Morota T, Honda C, Demura H, Kitazato K, Terazono J, Asada N (2011) The widespread occurrence of high-calcium pyroxene in bright-ray craters on the Moon and implications for lunar-crust composition. Geophys Res Lett 38:L17202

O'Hara MJ, Niu YL (2015) Obvious problems in lunar petrogenesis and new perspectives. *In:* Foulger GR, Lustrino M, King SD (eds). The Interdisciplinary Earth: A Volume in Honor of Don L. Anderson. F Geol Soc Am Spec Paper 514 and Am Geophys Union Spec Publ 71:339–366

Ohtake M, Matsunaga T, Haruyama J, Yokota Y, Morota T, Honda C, Ogawa Y, Torii M, Miyamoto K, Arai T, Hirata N, Iwasaki A, Nakamura R, Hiroi T, Sugihara T, Takeda H, Otake H, Pieters CM, Saiki K, Kitazato K, Abe M, Asada N, Demura H, Yamaguchi Y, Sasaki S, Kodama S, Terazono J, Shirao M, Yamaji A, Minami S, Akiyama H, Jossett JL (2009) The global distribution of pure anorthosite on the Moon. Nature 461:236–241

Ohtake M, Takeda H, Matsunaga T, Yokota Y, Haruyama J, Morota T, Yamamoto S, Ogawa Y, Hiroi T, Karouji Y, Saiki K, Lucey PG (2012) Asymmetric crustal growth on the Moon indicated by primitive farside highland materials. Nat Geosci 5:384–388

O'Neill HStC (1991) The origin of the Moon and the early histroy of the Earth – A chemical model. Part 1: The Moon. Geochim Cosmochim Acta 55:1135–1157

Papanastassiou DA, Wasserburg GJ (1975) Rb–Sr study of a lunar dunite and evidence for early lunar differentiates. Proc Lunar Planet Sci Conf 8:1467–1489

Papike JJ, Ryder G, Shearer CK (1998) Lunar samples. Rev Mineral Geochem 36:5.1–5.234

Parmentier EM, Zhong S, Zuber MT (2002) Gravitational differentiation due to initial chemical stratification: Origin of lunar asymmetry by the creep of dense KREEP. Earth Planet Sci Lett 201:473–480

Peplowski PN, Beck AW, Lawrence DJ (2016) Geochemistry of the lunar highlands as revealed by measurements of thermal neutrons. J Geophys Res Planets 121:388–401

Pernet-Fisher JR, Joy KH (2016) The lunar highlands: old crust, new ideas. Astron Geophys 57:1.26–1.30

Pernet-Fisher JF, Deloule E, Joy KH (2019) Evidence of chemical heterogeneity within lunar anorthosite parental magmas. Geochim Cosmochim Acta 266:109–130

Pidgeon RT, Nemchin AA, van Bronswijk W, Geisler T, Meyer C, Compston W, Williams IS (2007) Complex history of a zircon aggregate from lunar breccia 73255. Geochim Cosmochim Acta 71:1370–1381

Piskorz D, Stevenson DJ (2014) The formation of pure anorthosite on the Moon. Icarus 239:238–243

Potter RWK, Collins GS, Keifer WS, McGovern PJ, Kring DA (2012) Constraining the size of the South Pole-Aitken Basin impact. Icarus 220:730–743

Premo WR, Tatsumoto M (1992) U–Th–Pb, Rb–Sr, and Sm–Nd isotopic systematics of lunar troctolitic cumulate 76535: Implications on the age and origin of this early lunar, deep-seated cumulate. Proc Lunar Planet Sci Conf 22:381–397

Prettyman TH, Hagerty JJ, Elphic RC, Feldman WC, Lawrence DJ, McKinney GW, Vaniman DT (2006) Elemental composition of the lunar surface: Analysis of gamma ray spectroscopy data from Lunar Prospector. J Geophys Res 111:E12007

Pritchard ME, Stevenson DJ (2000) Thermal implication of lunar origin by Giant Impact. *In:* Canup RM, Tucson RK (eds) Origin of the Earth and Moon, The University of Arizona Press, p 179–196

Qin L, Alexander CMD, Carlson RW, Horan MF, Yokoyama T (2010) Contributors to chromium isotope variation of meteorites. Geochim Cosmochim Acta 74:1122–1145

Rai N, van Westrenen W (2014) Lunar core formation: New constraints from metal–silicate partitioning of siderophile elements. Earth Planet Sci Lett 388:343–352

Rankenburg K, Brandon AD, Neal CR (2006) Neodymium isotope evidence for a chondritic composition of the Moon. Science 312:1369–1372

Rapp JF, Draper DS (2018) Fractional crystallization of the lunar magma ocean: Updating the dominant paradigm. Meteorit Planet Sci 53:1432–1455

Raterron P, Holyoke C, Tokle L, Hilairet N, Merkel S, Hirth G, Weidner D (2017) Effect of iron content on olivine viscosity and implications for the Martian mantle. Lunar Planet Sci Conf 48:1553

Ricolleau A, Fei Y, Corgne A, Siebert J, Badro J (2011) Oxygen and silicon contents of the Earth's core from high pressure metal–silicate partitioning experiments. Earth Planet Sci Lett 310:409–421

Righter K (2002) Does the Moon have a metallic core?: Constraints from giant impact modeling and siderophile elements. Icarus 158:1–13

Righter K (2003) Metal–silicate partitioning of siderophile elements and core formation in the early Earth. Annu Rev Earth Planet Sci 31:135–174

Righter K, Go BM, Pando KA, Danielson L, Ross DK, Rahman Z, Keller LP (2017) Phase equilibriua of a low S and C lunar core: Implications for an early lunar dynamo and physical state of the current core. Earth Planet Sci Lett 463:323–332
Ringwood AE, Seifert S, Waenke H (1987) A komatiite component in the Apollo 16 highland breccias: implications for the nickel–cobalt systematics and bulk composition of the Moon. Earth Planet Sci Lett 81:105–117
Russell SS, Joy KH, Jeffries TE, Consolmagno GJ, Kearsley A (2014) Heterogeneity in lunar anorthosite meteorites: implications for the lunar magma ocean model. Phil Trans R Soc Ser A 372:20130241
Sato H, Robinson MS, Lawrence SJ, Denevi BW, Hapke B, Jolliff BL, Hiesinger H (2017) Lunar mare TiO_2 abundances estimated from UV/Vis reflectance. Icarus 296:216–238
Scott T, Kohlstedt DL (2006) The effect of large melt fration on the deformation behavior of peridotite. Earth Planet Sci Lett 246:177–187
Shearer CK, Papike JJ (1999) Magmatic evolution of the Moon. Am Mineral 84:1469–1494
Shearer CK, Papike JJ (2005) Early crustal building processes on the moon: Models for the petrogenesis of the magnesian suite. Geochim Cosmochim Acta 69:3445–3461
Shearer CK, Hess PC, Wieczorek MA, Pritchard ME, Parmentier EM, Borg LE, Longhi J, Elkins-Tanton LT, Neal CR, Antonenko I, Canup RM, Halliday AN, Grove TL, Hager BH, Lee D-C, Wiechert U (2006) Thermal and magmatic evolution of the Moon. Rev Mineral Geochem 60:365–518
Shearer CK, Elardo SM, Petro NE, Borg LE, McCubbin FM (2015) Origin of the lunar highlands Mg-suite: An integrated petrology, geochemistry, chronology, and remote sensing perspective. Am Mineral 100:294–325
Shearer C, Neal CR, Glotch TD, Prissel TC, Bell AS, Assis Fernandes V, Gaddis LR, Jolliff BL, Laneuville M, Magna T, Simon J (2023) Magmatic evolution II: A new view of post-differentiation magmatism. Rev Mineral Geochem 89:147–205
Shih C-Y, Nyquist LE, Bogard DD, Wooden JL, Bansal B, Wiesmann (1985) Chronology and petrogenesis of a 1.8 g lunar granitic clast: 14321,1062. Geochim Cosmochim Acta 49:411–426
Shih CY, Nyquist LE, Dasch EJ, Bogard DD, Bansal BM, Wiesmann H (1993) Ages of pristine noritic clasts from lunar breccias 15445 and 15455. Geochim Cosmochim Acta 57:915–931
Siegler MA, Miller RS, Keane JT, Laneuville M, Paige DA, Matsuyama I, Lawrence DJ, Crotts A, Poston MJ (2017) Lunar true polar wander inferred from polar hydrogen. Nature 531:480–484
Simon SB, Papike JJ (1985) Petrology of the Apollo 12 highland component. J Geophys Res Solid Earth 90:47–60
Sio CK, Borg LE, Cassata WS (2020) The timing of lunar solidification and mantle overturn recorded in ferroan anorthosite 62237. Earth Planet Sci Lett 538:116219
Smith JV, Anderson AT, Newton RC, Olsen EJ, Crewe AV, Isaacson MS, Johnson D, Wyllie PJ (1970) Petrologic history of the moon inferred from petrography, mineralogy and petrogenesis of Apollo 11 rocks. Geochim Cosmochim Acta 1:897
Snape JF, Nemchin AA, Bellucci JJ, Whitehouse MJ, Tartèse R, Barnes JJ, Anand M, Crawford IA, Joy KH (2016) Lunar basalt chronology, mantle differentiation and implications for determining the age of the Moon. Earth Planet Sci Lett 451:149–158
Snyder GA, Taylor LA, Neal CR (1992) A chemical model for generating the sources of mare basalts: Combined equilibrium and fractional crystallization of the lunar magmasphere. Geochim Cosmochim Acta 56:3809–3823
Snyder GA, Taylor LA, Halliday AN (1995) Chronology and petrogenesis of the lunar highlands suite: Cumulates from KREEP basalt crystallization. Geochim Cosmochim Acta 59:1185–1203
Solomatov VS (2000) Fluid dynamics of a terrestrial magma ocean. *In*: Canup RM, Righter K (eds). Origin of the Earth and Moon. University of Arizona Press, Phoenix
Solomatov VS (2007) Magma oceans and primordial mantle differentiation. Treatise on Geophysics 9:91–120
Solomon SC, Longhi J (1977) Magma oceanography: 1. Thermal evolution. Proc. 8th Lunar Sci Conf, p 583–599
Sprung P, Keline T, Scherer EE (2013) Isotopic evidence for chondritic Lu/Hf and Sm/Nd of the Moon. Earth Planet Sci Lett 380:77–87
Spudis PD, Reisse RA, Gillis JJ (1994) Ancient multiring basins on the Moon revealed by Clementine laser altimetry. Science 266:1848–1851
Spudis PD, Wilhelms DE, Robinson MS (2011) Sculptured Hills: Implications for the relative age of Serenitatis, basin chronologies, and the cratering history of the Moon. J Geophys Res 116:E00H03
Steenstra ES, van Westrenen W (2016) Siderophile elements in the lunar mantle. *In*: Cudnik B (ed) Encyclopedia of Lunar Science. Springer, Cham
Steenstra ES, van Westrenen W (2017) Lunar core formation. *In*: Cudnik B (ed) Encyclopedia of Lunar Science. Springer, Cham
Steenstra ES, Lin Y, Rai N, Jansen M, van Westrenen W (2017) Carbon as the dominant light element in the lunar core. Am Mineral 102:92–97
Steenstra ES, Berndt J, Klemme S, Fei Y, van Westrenen W (2020) A possible high-temperature origin of the Moon and its geochemical consequences. Earth Planet Sci Lett 538:116222
Steenstra ES, Rai N, Knibbe JS, Lin YH, van Westrenen W (2016) New geochemical models of core formation in the Moon from the metal–silicate partitioning of 15 siderophile elements. Earth Planet Sci Lett 441:1–9
Stuart-Alexander D (1978) Geologic map of the central far side of the Moon, USGS Map 1–1047
Suckale J, Sethian JA, Yu J-D, Elkins-Tanton LT (2012a) Crystals stirred up: 1. Direct numerical simulations of crystal settling in nondilute magmatic suspensions. J Geophys Res 117:E08004

Suckale J, Elkins-Tainton LT, Sethian JA (2012b) Crystals stirred up: 2. Numerical insights into the formation of the earliest crust on the Moon. J Geophys Res 117:E08005

Sun C, Liang Y (2013) Distribution of REE and HFSE between low-Ca pyroxene and lunar picritic melts around multiple saturation points. Geochim Cosmochim Acta 119:340–358

Sun C, Graff M, Liang Y (2017) Trace element partitioning between plagioclase and silicate melt: The importance of temperature and plagioclase composition, with implications for terrestrial and lunar magmatism. Geochim Cosmochim Act 206:273–295

Takeda H, Yamaguchi A, Bogard DD, Karouji Y, Ebihara M, Ohtake M, Saiki K, Arai T (2006) Magnesian anorthosites and a deep crustal rock from the farside crust of the moon. Earth Planet Sci Lett 247:171–184

Tartèse R, Anand M, Gattacceca J, Joy KH, Mortimer JI, Pernet-Fisher JF, Russell S, Snape JF, Weiss BP (2019) Constraining the evolutionary history of the moon and the inner solar system: a case for new returned lunar samples. Space Sci Rev 215:54

Tasaka M, Zimmerman ME, Kohlstedt DL (2015) Creep behavior of Fe-bearing olivine under hydrous conditions. J Geophys Res: Solid Earth 120:6039–6057

Taylor SR (1982) Planetary Science: A Lunar Perspective. Houston, Texas: Lunar and Planetary Institute

Taylor SR, McLennan S (2009) Planetary Crusts: their Composition, Origin and Evolution (Vol. 10). Cambridge University Press

Taylor SR, Taylor GJ, Taylor LA (2006) The Moon: a Taylor perspective. Geochim Cosmochim Acta 70:5904–5918

Taylor DJ, McKeegan KD, Harrison TM (2009) Lu–Hf zircon evidence for rapid lunar differentiation. Earth Planet Sci Lett 279:157–164

Tera F, Wasserburg GJ (1974) U–Th–Pb systematics on lunar rocks and inferences about lunar evolution and the age of the Moon. Proc 5th Lunar Sci Conf, p 1571–1599

Thacker C, Liang Y, Peng Q, Hess P (2009) The stability and major element partitioning of ilmenite and armalcolite during lunar cumulate mantle overturn. Geochim Cosmochim Acta 73:820–836

Tikoo SM, Weiss BP, Cassata WS, Shuster DL, Gattacceca J, Lima EA, Suavet C, Nimmo F, Fuller MD (2014) Decline of the lunar core dynamo. Earth Planet Sci Lett 404:89–97

Till JL, Moskowitz B (2013) Magnetite deformation mechanism maps for better prediction of strain partitioning. Geophys Res Lett 40:697–702

Tokle L, Hirth G, Raterron P, Dygert N, Liang YCW, Holyoke CW (2017) the pressure and Mg# dependence of ilmenite and ilmenite–olivine aggregate rheology: implications for lunar cumulate mantle overturn. Lunar Planet Sci Conf 48:2070

Tonks WB, Melosh HJ (1990) The physics of crystal settling and suspension in a turbulent magma ocean. Origin of the Earth 1:151–174

Touboul M, Kleine T, Bourdon B, Palme H, Wieler R (2007) Late formation and prolonged differentiation of the Moon inferred from W isotopes in lunar metals. Nature 450:20–27

Touboul M, Puchtel IS, Walker RJ (2015) Tungsten isotopic evidence for disproportional late accretion to the Earth and Moon. Nature 520:530–533

Treiman AH, Maloy AK, Shearer CK Jr, Gross J (2010) Magnesian anorthositic granulites in lunar meteorites in lunar meteorites Allan Hills 81005 and Dhofar 309: Geochemistry and global significance. Meteorit Planet Sci 45:163–180

Tsunakawa H, Shibuya H, Takahashi F, Shimizu H, Matsushima M, Matsuoka A, Nakazawa S, Otake H, Lijima Y (2010) Lunar magnetic field observation and initial global mapping of lunar magnetic anomalies by MAP-LMAG onboard SELENE (Kaguya). Space Sci Res 154:219–251

Vander Kaaden KE, Agee CB, McCubbin FM (2015) Density and compressibility of the molten lunar picritic glasses: Implications for the roles of Ti and Fe in the structures of silicate melts. Geochim Cosmochim Acta 149:1–20

Van Kan Parker M, Mason PRD, van Westrenen W (2011a) Experimental study of trace element partitioning between lunar orthopyroxene and anhydrous silicate melt: effects of lithium and iron. Chem Geol 285:1–14

Van Kan Parker M, Mason PRD, van Westrenen W (2011b) Trace element partitioning between ilmenite, armalcolite and anhydrous silicate melt: Implications for the formation of lunar high-Ti mare basalts. Geochim Cosmochim Acta 75:4179–4193

Van Kan Parker M, Sanloup C, Sator N, Guillot B, Tronche EJ, Perrillat J-P, Mezouar M, Rai N, van Westrenen W (2012) Neutral buoyancy of titanium-rich melts in the deep lunar interior. Nat Geosci 5:186–189

Vaughan WM, Head JW (2013), Modeling the South Pole-Aitken Basin subsurface. Lunar Planet Sci Conf 44:2012

Vaughan WM, Head JW (2014) Impact melt differentiation in the South Pole-Aitken basin: Some observations and speculations. Planet Space Sci 91:101–106

Villiger S, Müntener O, Ulmer P (2007) Crystallization pressures of mid-ocean ridge basalts derived from major element variations of glasses from equilibrium and fractional crystallization experiments. J Geophys Res: Solid Earth 112:B01202

Walker D (1983) Lunar and terrestrial crust formation. J Geophys Res 88:B17–B25

Walker D, Hays JF (1977) Plagioclase flotation and lunar crust formation. Geology 5:425–428

Walker D, Longhi J, Hays J (1975) Differentiation of a very thick magma body and implications for the source region of mare basalts. Proc 6th Lunar Sci Conf, p 1103–1120

Wänke H, Palme H, Baddenhausen H, Dreibus G, Jagoutz E, Kruse H, Spettel B, Teschke F, Thacker R (1974) Chemistry of Apollo 16 and 17 samples: bulk composition, late stage accumulation and early differentiation of the Moon. Proc Lunar Sci Conf 5th, p 1307–1335
Warren PG (1985) The magma ocean concept and lunar evolution. Annu Rev Earth Planet Sci 13:201–240
Warren PG (1990) Lunar anorthosites and the magma-ocean plagioclase-floatation hypothesis: Importance of FeO enrichment in the parent magma. Am Mineral 75:46–58
Warren PG (1989) KREEP: major-element diversity, trace element uniformity (almost). *In:* Workshop on Moon in Transition: Apollo 14, KREEP, and Evolved Lunar Rocks, LPI Technical Report Number 89-03, p 149–153
Warren P, Wasson J (1979) The compositional-petrographic search for pristine nonmare rocks—Third foray. Proc Lunar Planet Sci Conf 10:583–610
Weber RC, Lin PY, Garnero EJ, Williams Q, Lognonné P (2011) Seismic detection of the lunar core. Science 331:309–312
Weiss BP, Tikoo SM (2014) The lunar dynamo. Science 346:1246753
Wetzel DT, Hauri EH, Saal AE, Rutherford MJ (2015) Carbon content and degassing history of the lunar volcanic glasses. Nat Geosci 8:755–758
Whitehead JA (1988) Fluid models of geological hotspots. Annu Rev Fluid Mech 20:61–87
Wieczorek MA (2009) The interior structure of the Moon: What does geophysics have to say? Elements 5:35–40
Wieczorek MA, Zuber MT (2001) The composition and origin of the lunar crust: Constraints from central peaks and crustal thickness models. Geophys Res Lett 28:4023–4026
Wieczorek MA, Neumann GA, Nimmo F, Kiefer WS, Taylor GJ, Melosh HJ, Phillips RJ, Solomon SC, Andrews-Hanna JC, Asmar SQ, Konopliv AS, Lemoine FG, Smith DE, Watkins MM, Williams JG, Zuber MT (2013) The crust of the Moon as seen by GRAIL. Science 339:671–675
Wieczorek MA, Weiss BP, Breuer D, Cébron D, Fuller M, Garrick-Bethell I, Gattacceca J, Halekas JS, Hemingway DJ, Hood LL, Laneuville M, Nimmo F, Oran R, Purucker ME, Rückriemen T, Soderlund KM, Tikoo1 SM (2023) Lunar magnetism. Rev Mineral Geochem 89:207–241
Williams JG, Boggs DH (2015) Tides on the Moon: Theory and determination of dissipation. J Geophys Res Planets 120:689–724
Williams JG, Boggs DH, Yoder CF, Ratcliff JT, Dickey JO (2001) Lunar rotational dissipation in solid body and molten core. J Geophys Res Planets 106:27933–27968
Williams JG, Konopliv AS, Boggs DH, Park RS, Yuan DN, Lemoine FG, Goossens S, Mazarico E, Nimmo F, Weber RC, Asmar SW (2014) Lunar interior properties from the GRAIL mission. J Geophys Res 119:1546–1578
Wood JA, Dickey JS, Marvin UB, Powell BN (1970) Lunar anorthosites. Science 167:602–604
Yamamoto S, Nakamura R, Matsunaga T, Ogawa Y, Ishihara Y, Morota T, Hirata N, Ohtake M, Hiroi T, Yokota Y, Haruyama J (2010) Possible mantle origin of olivine around lunar impact basins detected by SELENE. Nat Geosci 3:533–536
Yamamoto S, Nakamura R, Matsunaga T, Ogawa Y, Ishihara Y, Morota T, Hirata N, Ohtake M, Hiroi T, Yokota Y, Haruyama J (2012) Massive layer of pure anorthosite on the Moon. Geophys Res Lett 39:L13201
Yamamoto K, Haruyama J, Kobayashi S, Ohtake M, Iwata T, Ishihara Y, Hasebe N (2016) Two-stage development of the lunar farside highlands crustal formation. Planet Space Sci 120:43–47
Yamashita N, Hasebe N, Reedy RC, Kobayashi S, Karouji Y, Hareyama M, Shibamura E, Kobayashi M-N, Okudaira O, d'Uston C, Gasnault O, Forni O, Kim KJ (2010) Uranium on the Moon: Global distribution and U/Th ratio. Geophys Res Lett 37:L10201
Young ED, Kohl IE, Warren PH, Rubie DC, Jacobson SA, Morbidelli A (2016) Oxygen isotopic evidence for vigorous mixing during the Moon-forming giant impact. Science 35:493–496
Yu S, Tosi N, Schwinger S, Maurice M, Breuer D, Xiao L (2019) Overturn of ilmenite-bearing cumulates in a rheologically weak lunar mantle. J Geophys Res: Planets 124:418–436
Zahnle KJ, Kasting JF, Pollack JB (1988) Evolution of a steam atmosphere during Earth's accretion. Icarus 74:62–97
Zhang J, Dauphas N, Davis AM, Leya I, Fedkin A (2012) The proto-Earth as a significant source of lunar material. Nat Geosci 5:251
Zhang N, Parmentier EM, Liang Y (2013a) A 3-D numerical study of the thermal evolution of the Moon after cumulate mantle overturn: The importance of rheology and core solidification. J Geophys Res: Planets 118:1789–1804
Zhang N, Parmentier EM, Liang Y (2013b) Effects of lunar cumulate mantle overturn and megaregolith on the expansion and contraction history of the Moon. Geophys Res Lett 40:5019–5023
Zhang N, Dygert N, Liang Y, Parmentier EM (2017) The effect of ilmenite viscosity on the dynamics and evolution of an overturned lunar cumulate mantle. Geophys Res Lett 44:6543–6552
Zhao Y, Zimmerman ME, Kohlstedt DL (2009) Effect of iron content on the creep behavior of olivine: 1. Anhydrous conditions. Earth Planet Sci Lett 287:229–240
Zhao Y, De Vries J, van den Berg AP, Jacobs MHG, van Westrenen W (2019) The participation of ilmenite-bearing cumulates in lunar mantle overturn. Earth Planet Sci Lett 511:1–11
Zhong S, Parmentier M, Zuber M (2000) A dynamic origin for the global asymmetry of lunar mare basalts. Earth Planet Sci Lett 177:131–140

APPENDIX—RECENT DEVELOPMENTS

Recent observations of KREEP-poor magnesian lunar meteorites and pink spinel troctolites with highly magnesian olivine (Fo96) have challenged the assumption that KREEP is a required component of Mg-suite magmatism (e.g., Gross et al. 2019) and suggest the possibility that at least some primary Mg-suite magmas originate as melts of primitive olivine-rich LMO cumulates (e.g., Prissel et al. 2016). However, the absence of significant exposures of olivine-rich mantle exposures argues against large-scale upwelling or transfer of primitive LMO cumulates to shallow depth during cumulate overturn (e.g., Yamamoto et al. 2010, Melosh et al. 2017). In order to constrain the petrogenesis of Mg-suite rocks (troctolites and norites), Prissel and Gross (2020) conducted petrogenetic modeling of lunar cumulate decompression melting during a cumulate pile overturn scenario followed by subsequent crystallization. Their results demonstrate feasible scenarios for producing parental melts for the Mg-suite without plagioclase assimilation or a hybridized mantle source such as are commonly invoked in Mg-suite petrogenetic models; paired with KREEP-poor magnesian lithologies in the lunar meteorite collection, their results support the hypothesis that KREEP is not a required component of Mg-suite petrogenesis. Instead, they propose a model in which partial melts of olivine-rich primitive LMO cumulates are formed by decompression melting during upwelling, and then extracted at depth without accompanying large-scale transfer of olivine-rich mantle to the upper layers of the Moon. This model accounts for the close temporal and chemical relationship between magma ocean crystallization and Mg-suite magmatism and is consistent with the presence of KREEP-poor, Mg-rich lithologies as well as the absence of large-scale olivine-rich exposures observed by remote sensing. Results are also consistent with previous studies challenging the proposed and long-standing genetic relationship between Mg-suite and gabbronorites.

REFERENCES

Melosh HJ, Kendall J, Horgan B, Johnson BC, Bowling T, Lucey PG, Taylor GJ (2017). South Pole-Aitken basin ejecta reveal the Moon's upper mantle. Geology 45:1063–1066

Prissel TC, Gross J (2020) On the petrogenesis of lunar troctolites: new insights into cumulate mantle overturn & mantle exposures in impact basins. Earth Planet Sci Lett 551:116531

Prissel TC, Parman SW, Head JW (2016) Formation of the Lunar Highlands Mg-suite as told by Spinel. Am Mineral 101:1624–1635

Yamamoto S, Nakamura R, Matsunaga T, Ogawa Y, Ishihara Y, Morota T, Hirata N, Ohtake M, Hiroi T, Yokota Y, Haruyama J (2010) Possible mantle origin of olivine around lunar impact basins detected by SELENE. Nat Geosci 3:533–536